Measurement of the B_s mass in $B_s \to J/\psi\phi \to \mu^+\mu^- K^+K^-$, and physics validation with J/ψ events in ATLAS

by

Maren Ugland

Master Degree Thesis in Experimental Particle Physics
Department of Physics and Technology
University of Bergen
Norway

September 25, 2008

Acknowledgements

First of all, I would like to thank my supervisor, Prof. Gerald Eigen, for his excellent comments and inputs for this thesis, and for his guidance throughout these last two years. Thank you for being available to answer all my questions, and for all you have taught me about particle physics.

Secondly, I would like to thank Trygve Buanes, for producing the root ntuples this analysis is performed on, and for helping me with some of my many programming problems along the way.

I would also like to thank my fellow students, Hilde Skjerdal, Therese Sjursen and Alex Kastanas, for many interesting physics debates, and for making the last two years memorable. A special thanks to Alex, for his magnificent IT support.

To Heidi Sandaker, for proofreading my theory chapters on short notice, and to Are Raklev, for his patience and his ability to ans-wear all questions in a simple manner: Thank you.

Last, but not least, I would like to thank my family and friends for all their love and support, and especially Eirik, for not giving up on me during the last two months. I couldn't have done this without you!

Maren Ugland

August 29, 2008

Preface

The main focus of this thesis is the study of the B_s mass in $B_s \to J/\psi\phi \to \mu^+\mu^- K^+ K^-$ decays in ATLAS. The study is performed on root ntuples made from the officially produced ATLAS data, containing 14,750 signal events and 184,175 background events. Two separate types of backgrounds are investigated: $i)$ Generic B decays, $bb \to \mu^+\mu^- X$, where the two muons may or may not come from a J/ψ, and $ii)$ direct J/ψ events, $pp \to J/\psi\mu^+\mu^- X$.

A separate study of physics validation is also preformed. Using 89,000 simulated $J/\psi \to \mu^+\mu^-$ events, we look for variations in the reconstructed J/ψ mass throughout the detector volume.

Chapter 1 explains the general aspects of the Standard Model of particle physics, the theoretical framework upon which this thesis is based, with emphasis on B-physics related topics.

The LHC accelerator complex, which is scheduled to produce the first proton-proton collisions only a few weeks from now, is described in Chapter 2. The chapter also gives a detailed description of the ATLAS detector, which we will use to observe the outcome of these collisions.

Chapter 3 introduces the analysis framework and the different data formats used within the ATLAS collaboration. It also gives a short description of how the simulated data is made.

Finally, Chapters 4 and 5 explains the details of the two respective analyses, while Chapter 6 sums up the obtained results and discusses future prospects.

Contents

List of Figures

List of Tables

Chapter 1

Theoretical Background

1.1 The Standard Model

> By convention sweet,
> by convention bitter,
> by convention hot,
> by convention cold,
> by convention colour:
> but in reality atoms and void.
>
> Democritus, Greek Philosopher, ca. 460 - 370 BC

The idea that all matter is made up of one or more fundamental particles, has existed for thousands of years. However, which particles that are considered fundamental has changed with time as physicists' knowledge has improved. The Standard Model (SM) of particle physics is today's basic theory of fundamental matter particles and their interactions [1]. It attempts to explain all the aspects of particle physics in terms of the properties and interactions of three different types of particles. The two kinds of matter particles, *leptons* and *quarks*, are spin-$\frac{1}{2}$ fermions, while the force carriers, the so-called *gauge bosons*, have spin-1. In the Standard Model all these particles are thought to be elementary. This means that they are treated as point particles, without internal structure or excited states. Table 1.1 gives an overview of the Standard Model matter particles and some of their properties.

1.1.1 The Matter Particles

The fermions are separated into three families, of which only the first is considered stable[1]; the particle masses increase with increasing family number. The first family is comprised of the quarks up (u) and down (d), which can be found in atomic nuclei, and the two leptons electron (e) and electron neutrino (ν_e). The second family consists of the

[1] A stable particle is by definition one that does not decay. The experimental lower bound on the electron lifetime for instance, is 4.6×10^{26} years [2].

Family number	Type	Particle	Spin	Charge
I	Lepton	e	$\frac{1}{2}$	-1
		ν_e	$\frac{1}{2}$	0
	Quark	u	$\frac{1}{2}$	$\frac{2}{3}$
		d	$\frac{1}{2}$	$-\frac{1}{3}$
II	Lepton	μ	$\frac{1}{2}$	-1
		ν_μ	$\frac{1}{2}$	0
	Quark	c	$\frac{1}{2}$	$\frac{2}{3}$
		s	$\frac{1}{2}$	$-\frac{1}{3}$
III	Lepton	τ	$\frac{1}{2}$	-1
		ν_τ	$\frac{1}{2}$	0
	Quark	t	$\frac{1}{2}$	$\frac{2}{3}$
		b	$\frac{1}{2}$	$-\frac{1}{3}$

Table 1.1: The Standard Model has three families of fundamental matter particles, with mostly the same properties. The mass increases with increasing family number. Only the first family of particles are stable.

charm quark (c), the strange quark (s), and the leptons muon (μ) and muon neutrino (ν_μ), both of which we can observe in cosmic rays. The third family consists of the quarks top (t) and bottom (b), and the leptons tau (τ) and tau neutrino (ν_τ). These are highly unstable and are only observed in high energy physics experiments.

In addition to electric charge, the quarks carry an extra degree of freedom, called colour charge (which can be red, green, or blue). However, the theory states that no coloured object can exist freely. Therefore the quarks combine and form colour-neutral bound states, called *hadrons*. A hadron can either consist of a quark-antiquark pair[2], called a *meson*, or three quarks of different colour, called a *baryon*.

All particles (elementary and composite) have an associated anti-particle with mostly the same properties, i.e. the same mass, spin, etc., but with opposite quantum charges. For example, the electrons anti-particle is the positron (e^+), which is produced naturally in certain types of radioactive decay. It has the same mass as the electron, but its electric charge is +1 (as opposed to the electrons charge of -1). Theoretically, anti-particles are a consequence of combining special relativity with quantum mechanics [1]. Bosons are their own anti-particles.

[2] The antiquark carries anti-colour, i.e. anti-red, anti-green, or anti-blue.

Gauge boson		Interaction
Symbol	Name	
γ	photon	Electromagnetic
Z^0	Z^0 boson	Weak
$W^{\pm}$	$W^{\pm}$ boson	
g	gluon	Strong

Table 1.2: The SM gauge bosons and the forces they mediate.

1.1.2 The Force Carriers and Their Interactions

In the Standard Model there are three types of forces: The electromagnetic, the weak and the strong force[3]. Leptons interact via the weak force and the electromagnetic force (only the charged leptons interact electromagnetically), while quarks also interact via the strong force. The interactions are described by a relativistic Quantum Field Theory (QFT)[4], which is a theoretical framework for constructing quantum mechanical models of many-body systems [4]. Table 1.2 gives an overview of the Standard Model gauge bosons and what interactions they mediate.

The electromagnetic force is mediated by massless photons, and is felt by all particles with electric charge or magnetic dipole moment. Since the photon is massless, the force has an infinite range, but its' strength decreases as $1/r^2$. The theory describing the electromagnetic interactions is called Quantum ElectroDynamics (QED). The weak force is mediated by the W^+/W^- and Z^0 boson. These are heavy particles (80.4 GeV and 91.2 GeV respectively), which means that the range is short, only 10^{-18} m. All fermions are affected by the weak force. The strong force is mediated by massless gluons and is described by Quantum CromoDynamics (QCD). It is felt by all particles with colour charge (quarks and gluons), and its range is 10^{-15} m, which is approximately the size of the proton radius. The reason for the range being so short, even though the gluons (like the photons) are massless, has to do with the fact that the gluons carry colour charge.

1.1.3 The Standard Model Gauge Groups

The Standard Model is formulated in a mathematical framework, which tries to explain the particle world in terms of symmetries and conservation laws. It is a local gauge theory, and is based on the symmetry group $SU(3)_C \times SU(2)_L \times U(1)_Y$, where the indices are C for colour, L for left-handed (refers to the *chirality* of the particle, i.e. the direction of

[3] Gravity is not included in the Standard Model due to its inferior strength and problems in combining general relativity, which is the best existing model to explain gravity, with the rest of the theory.

[4] An in-dept introduction to QFT can be found in [3].

its' spin compared to the momentum) and Y for hypercharge. In addition to the internal symmetries of quantum charges – colour, weak, hypercharge – the external space-time symmetries, i.e. those of translations, rotations and boosts (changes of velocity), have been central to the development of the Standard Model [5].

When working with symmetries, the language is that of abstract algebraic operators working on states that represent elementary particles or systems of particles. A *unitary group* U(n), is a group of complex valued $n \times n$ *unitary* matrices. A unitary matrix U, is a matrix whose inverse is its hermitian conjugate, i.e.

$$U^\dagger U = I \ , \tag{1.1}$$

where I is the identity matrix. A *special unitary group* SU(n) is a unitary group that in addition satisfies

$$\det U = 1 \ . \tag{1.2}$$

Most groups are non-abelian, meaning that the group's operators do not commute. The exception is U(1), which consists of the complex numbers of unit length.

Any element U in U(n) has a *representation* in terms of a Hermitian matrix M:

$$U = e^{iM} \quad \text{where} \quad M^\dagger = M \ , \tag{1.3}$$

where the dimension of M gives the dimension of the representation. For SU(n) it is in addition required that M is a traceless matrix, i.e. that Tr M = 0.

The *generators* of a group G are the set of operators M_i, such that any element of G can be written

$$U = e^{iM^i\theta^i} \ , \tag{1.4}$$

where θ^i are in general complex parameters. The generators of a group is what defines the algebra of the group.

The strong force is described by the SU(3) gauge group, while the description of the weak and electromagnetic forces were unified in the sixties by S. Glashow, S. Weinberg and A. Salam [6, 7, 8, 9]. The resulting *electroweak theory* (EW) is described by the SU(2)$_L$×U(1)$_Y$ symmetry group.

As the SU(2) subscript L implies, the weak force only acts on left-handed particles (and right-handed anti-particles). This means that the left-handed particles can be grouped into doublets, while the right-handed particles are singlets under the weak interaction (i.e. they cannot transform into one another):

$$\begin{pmatrix} u \\ d \end{pmatrix}_L \ , \begin{pmatrix} c \\ s \end{pmatrix}_L \ , \begin{pmatrix} t \\ b \end{pmatrix}_L \ , u_R \ , c_R \ , t_R \ , d_R \ , s_R \ , b_R \ . \tag{1.5}$$

In principle the leptons can also be grouped in a similar way, though this is not incorporated in the Standard Model due to the fact that at the time when the theory was developed, the neutrinos were thought to be massless. Since that time, one has discovered that neutrinos can oscillate from one flavour state to another, which is only possible if they have non-zero masses.

1.1.4 The Higgs Mechanism

Gauge invariance of the theory implies that all particles involved have zero masses, which is contrary to what we observe experimentally. The masses are introduced by interactions with a *Higgs field* [10, 11, 12]. The simplest possibility is to introduce one SU(2) doublet of scalar fields (a scalar Higgs doublet, ϕ). Its self-interactions provide a mechanism for spontaneously breaking the SU(2) $\times$ U(1) symmetry, giving masses to the fermions and gauge bosons[5]. It also gives rise to a new scalar particle, the *Higgs boson* (H), which has not yet been observed despite extensive searches. One of the main goals of the LHC is in fact to discover this particle.

1.1.5 Shortcomings of the Standard Model

The Standard Model has proven to be an extremely successful theory, and has predicted a number of experimental results, e.g. the existence and masses of the $W^{\pm}$ and Z^0 boson, but there are some things it is not able to explain. We have already mentioned gravity and neutrino oscillations, though the latter could in principle be incorporated in the existing theory. Other (larger) problems include the matter–anti-matter asymmetry in the universe, the existence of dark matter and dark energy, the Hierarchy problem, the strong CP problem, and the problem of the cosmological constant. The Hierarchy problem and the strong CP problem are both related to problems of fine-tuning, which means that the parameters of the theory must be adjusted very precisely in order for it to agree with the experimental observations. In addition, the Hierarchy problem also suffers from a lack of naturalness. The problem of the cosmological constant is that the small experimental value deviates many orders of magnitude from the value predicted by QFT.

As we shall see in the upcoming sections, B-physics is especially important in constraining the Standard Model and in determining limits for new physics.

1.2 The CKM Matrix

The eigenstates of the weak interaction (d', s', b') are not the same as the mass eigenstates (d, s, b) obtained via the Higgs mechanism, but rather linear superpositions of them. The relation between the states is described by the Cabibbo-Kobayashi-Maskawa (CKM) mixing matrix [13, 14], where the elements express the probability for weak transitions within a doublet. By convention, the mixing is ascribed completely to the $q_e = -\frac{1}{3}$ states:

$$\begin{pmatrix} u \\ d' \end{pmatrix}_L \quad \begin{pmatrix} c \\ s' \end{pmatrix}_L \quad \begin{pmatrix} t \\ b' \end{pmatrix}_L , \tag{1.6}$$

[5] The fermion masses are obtained via Yukawa interactions with the Higgs field, while the gauge boson fields absorb the scalar fields as longitudinal components, giving rise to the gauge boson masses.

with

$$\begin{pmatrix} d' \\ s' \\ b' \end{pmatrix}_L = V \begin{pmatrix} d \\ s \\ b \end{pmatrix}_L , \tag{1.7}$$

and

$$V = \begin{pmatrix} V_{ud} & V_{us} & V_{ub} \\ V_{cd} & V_{cs} & V_{cb} \\ V_{td} & V_{ts} & V_{tb} \end{pmatrix} . \tag{1.8}$$

The CKM matrix, V, is a unitary matrix, meaning that $VV^\dagger = 1$, where $V^\dagger$ describes the mixing between anti-quarks. As a consequence of unitarity, we find that the matrix can be parameterized by four independent variables: Three mixing angles and one CP-violating phase[6]. The standard (Maiani) representation [15] is

$$V_{CKM} = \begin{pmatrix} c_1c_3 & s_1c_3 & s_3e^{-i\delta} \\ -s_1c_2 - c_1s_2s_3e^{i\delta} & c_1c_2 - s_1s_2s_3e^{i\delta} & s_2c_3 \\ s_1s_2 - c_1c_2s_3e^{i\delta} & -c_1s_2 - s_1c_2s_3e^{i\delta} & c_2c_3 \end{pmatrix} , \tag{1.9}$$

where $s_i \equiv \sin\theta_i$, and $c_i \equiv \cos\theta_i$.

1.2.1 The Small-Angle Wolfenstein Parameterization

Because of the fact that the size of the angles, θ_i, of the Maiani parameterization are known to have a hierarchical pattern ($s_3 << s_2 << s_1$), it is useful to parameterize the CKM matrix in the following way [16]:

$$V_{CKM} = \begin{pmatrix} 1 - \lambda^2\backslash 2 & \lambda & A\lambda^3(\rho - i\eta) \\ -\lambda & 1 - \lambda^2\backslash 2 & A\lambda^2 \\ A\lambda^3(1 - \rho - i\eta) & -A\lambda^2 & 1 \end{pmatrix} + O(\lambda^4), \tag{1.10}$$

where λ corresponds essentially to the Cabibbo angle, $\lambda \simeq 0.22$, and η carries the information about the CP-violation. The Equation (1.10) is called the small-angle Wolfenstein parameterization [16], and is in particular used for B-physics. It can be obtained from the standard (Maiani) parameterization by assuming[7] that $s_3 << s_2 << s_1 << 1$, and making the replacements [2]

$$\begin{aligned} s_1 &= \lambda , \\ s_3e^{i\delta} &= A\lambda^3(\rho + \eta) , \\ s_2 &= A\lambda^2 . \end{aligned} \tag{1.11}$$

These equations also help define the last two parameters, A and ρ, which have no direct physical meaning

[6] CP violation is explained in Section 1.3

[7] The assumption is verified by experimental data

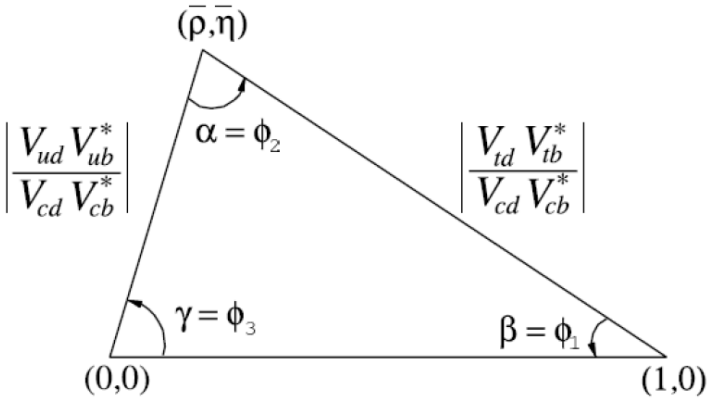

Figure 1.1: Sketch of the rescaled unitarity triangle [2].

1.2.2 Unitarity Relations

The unitarity of the CKM matrix can be represented as triangles in a complex plane. One can construct six such triangles (of equal area), but the most experimentally accessible, and hence most commonly used, is that which has come to be known as the *unitarity triangle* (see Figure 1.1). It arises from

$$V_{ud}V_{ub}^* + V_{cd}V_{cb}^* + V_{td}V_{tb}^* = 0 \,, \tag{1.12}$$

and can be rescaled by dividing each side by $V_{cd}V_{cb}^*$. The coordinates of the vertices are exactly (0,0), (1,0) and $(\bar{\rho},\bar{\eta})$, where

$$\bar{\rho} = \rho(1 - \frac{1}{2}\lambda^2) \text{ and } \bar{\eta} = \eta(1 - \frac{1}{2}\lambda^2) \,. \tag{1.13}$$

The angles of the unitarity triangle are

$$\beta = \phi_1 = \arg\left(-\frac{V_{cd}V_{cb}^*}{V_{td}V_{tb}^*}\right) \,,\; \alpha = \phi_2 = \arg\left(-\frac{V_{td}V_{tb}^*}{V_{ud}V_{ub}^*}\right) \,,\; \gamma = \phi_3 = \arg\left(-\frac{V_{ud}V_{ub}^*}{V_{cd}V_{cb}^*}\right) \,. \tag{1.14}$$

Many measurements of CP-violating processes can be used to constrain the angles, which provides an important test of the Standard Model. Thus far it has proven to be consistent up to an order $O(0.1)$, meaning that possible new physics theories should be thought of as corrections to the Standard Model rather than completely new theories to replace it.

1.2.3 Determination of the CKM Elements

An important goal of B-physics is to overconstrain the Standard Model. To accomplish this, the CKM parameters have to be measured with as high precision as possible. Often

several measurements, exploiting different physics processes, are made, and the results are then averaged over. In general, the simplest procedure is to study semileptonic decays, $q \rightarrow q' l \nu$, whose decay rate is proportional to $|V_{qq'}|^2$. However, the elements $|V_{td}|$ and $|V_{ts}|$ are determined from $B - \bar{B}$ mixing and loop-mediated rare K or B meson decays, and $|V_{tb}|$ can only be estimated from top quark decays. Equation (1.15) lists the best measurements obtained thus far [17]. They are all in agreement with unitarity.

$$\begin{aligned} V_{CKM} &= \begin{pmatrix} V_{ud} & V_{us} & V_{ub} \\ V_{cd} & V_{cs} & V_{cb} \\ V_{td} & V_{ts} & V_{tb} \end{pmatrix} \\ &= \begin{pmatrix} 0.97419 \pm 0.00022 & 0.2257 \pm 0.0010 & 0.00359 \pm 0.00016 \\ 0.2256 \pm 0.0010 & 0.97334 \pm 0.00023 & 0.0415^{+0.0010}_{-0.0011} \\ 0.00874^{+0.00026}_{-0.00037} & 0.0407 \pm 0.0010 & 0.999133^{+0.000044}_{-0.000043} \end{pmatrix} \end{aligned} \tag{1.15}$$

1.3 CP Violation and Mixing in Neutral Meson Systems

As previously mentioned, CP violation is important in the determination of the CKM angles, and hence in constraining the Standard Model. The phenomenon also helps explain some of the still unanswered questions of the model (see Section 1.1.5), e.g. why there exists a matter–anti-matter asymmetry in the universe. The general aspects of CP violation is in the following therefore introduced, starting with the symmetries of charge conjugation and parity:

The *parity operation*, P, changes the sign of the spatial coordinates of a wave function:

$$\hat{P}\psi(\mathbf{x}, t) = \eta_p \psi(-\mathbf{x}, t) \, , \tag{1.16}$$

where the eigenvalues η_p must be either +1 or -1. The corresponding wave functions are said to have even (+) or odd (-) parity. Both the strong and the electromagnetic interaction are thought to be invariant under the parity operation, while the weak force violates parity maximally. This means that particles with different chiralities are treated differently under the weak interaction.

Charge conjugation (or C-parity), C, replaces all particles by their anti-particles in the same state, so that momenta, positions, spins etc. remains unchanged:

$$\hat{C}\psi(\mathbf{x}, t) = \eta_c \overline{\psi}(\mathbf{x}, t) \, , \tag{1.17}$$

where the eigenvalues η_c must be either +1 or -1. Like parity, charge conjugation invariance is a symmetry of the strong and electromagnetic interaction, but is violated by the weak interaction. Invariance under charge conjugation means that particles and anti-particles are treated in the same way.

Time reversal, T, changes the sign of the time component:

$$\hat{T}\psi(\mathbf{x}, t) = \psi^*(\mathbf{x}, -t) \, . \tag{1.18}$$

Also it is a symmetry of the strong and electromagnetic interactions, and is violated by the weak interaction.

Though charge conjugation and parity separately are not invariant under the weak interaction, the combination, CP (or PC), is almost invariant also under the weak interaction[8]. It was however, observed experimentally already in 1964 in the K^0 meson system [18, 19], and recently it has also been observed in B^0 decays [20, 21]. CP violation in meson decays is currently our only evidence for the CP violation needed to explain the matter–anti-matter asymmetry in the universe.

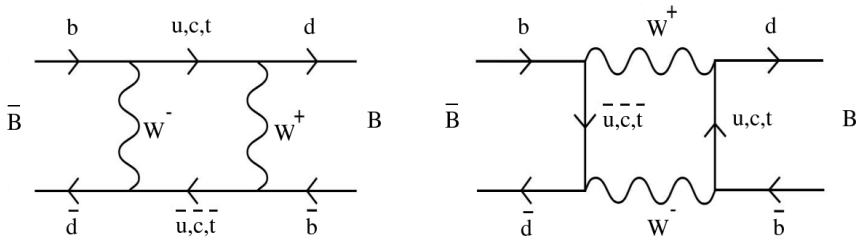

Figure 1.2: Feynman diagrams of $B^0 - \bar{B}^0$ mixing mediated by a double W exchange.

The neutral mesons (K^0, B^0, D^0) can oscillate into their anti-particle via a double W exchange (see Fig. 1.2). The time evolution of these oscillations can be described by a non-diagonal Hamiltonian matrix. The following example is for the case of neutral B mesons [22]:

$$H\begin{pmatrix} B^0 \\ \bar{B}^0 \end{pmatrix} = \begin{pmatrix} M - \frac{i}{2}\Gamma & M_{12} - \frac{i}{2}\Gamma_{12} \\ M^*_{12} - \frac{i}{2}\Gamma^*_{12} & M - \frac{i}{2}\Gamma \end{pmatrix}\begin{pmatrix} B^0 \\ \bar{B}^0 \end{pmatrix} \tag{1.19}$$

We have here assumed CPT invariance[9] to get $M_{11} = M_{22} = M$ and $\Gamma_{11} = \Gamma_{22} = \Gamma$. This means that the masses and lifetimes of particles and anti-particles are identical. Due to the Hermitian nature of M and Γ, we have also substituted $M_{21} = M^*_{12}$ and $\Gamma_{21} = \Gamma^*_{12}$ in the equation.

By diagonalizing the Hamiltonian we obtain the weak eigenstates

$$\begin{aligned} |B_1\rangle &= p|B^0\rangle + q|\bar{B}^0\rangle \\ |B_2\rangle &= p|B^0\rangle - q|\bar{B}^0\rangle \end{aligned}, \tag{1.20}$$

where

$$\frac{q}{p} = \sqrt{\frac{M^*_{12} - \frac{i}{2}\Gamma^*_{12}}{M_{12} - \frac{i}{2}\Gamma_{12}}}\,. \tag{1.21}$$

The weak eigenstates are often labeled L (light) and H (heavy) instead of 1 and 2. Light and heavy refers to the large mass difference between the two eigenstates[10]

[8] Experimental observations show no evidence of CP violation under strong or electromagnetic interactions.

[9] There are strong theoretical reasons to believe CPT transformations are invariant under all interactions.

[10] In the K^0 system they are often called S (short) and L (long) because of the lifetime difference of the two particle states.

To be invariant, the CP eigenstates have to satisfy

$$CP|B_1\rangle = +|B_1\rangle \ , \ CP|B_2\rangle = -|B_2\rangle \ . \tag{1.22}$$

This leads to the CP eigenstates

$$\begin{aligned} |B_1\rangle &= \frac{1}{\sqrt{2}}\left(|B^0\rangle - |\bar{B}^0\rangle\right) \\ |B_2\rangle &= \frac{1}{\sqrt{2}}\left(|B^0\rangle + |\bar{B}^0\rangle\right) \ . \end{aligned} \ , \tag{1.23}$$

which coincide with the weak eigenstates only if $q/p = 1$. If this is not the case, we have *CP violation in mixing*, or indirect CP violation. Another type of CP violation is *CP violation in decay*, also called direct CP violation. This involves different decay amplitudes, $A = \langle f|H|i\rangle$, for decays of B^0 ($\bar{B}^0$) into CP eigenstates f_{CP} ($\bar{f}_{CP}$). For any final state f, the ratio of the decay amplitudes $\left|\frac{\bar{A}_{\bar{f}_{CP}}}{A_{f_{CP}}}\right|$ is independent of phase conventions:

$$\left|\frac{\bar{A}_{\bar{f}_{CP}}}{A_{f_CP}}\right| = \left|\frac{\sum_i A_i \exp(i(\delta_i - \phi_i))}{\sum_i A_i \exp(i(\delta_i + \phi_i))}\right| \ , \tag{1.24}$$

where δ_i is a strong phase, while ϕ_i is a weak phase. If CP is not conserved then two of the terms in 1.24 have different weak phases and different strong phases, and $\left|\frac{\bar{A}_{\bar{f}_{CP}}}{A_{f_C P}}\right| \neq 1$.

We can also have CP violation as an interference between direct and indirect CP violation. In this case

$$\lambda = \eta_{CP}\frac{q}{p}\frac{\bar{A}_{\bar{f}_{CP}}}{A_{f_{CP}}} \neq \pm 1 \ , \tag{1.25}$$

where η_{CP} is the intrinsic CP of the CP eigenstate. The most interesting case is when both q/p and $\bar{A}_{\bar{f}_{CP}}/A_{f_{CP}}$ are equal to one, which gives $|\lambda| = 1$, but $\mathrm{Im}(\lambda) \neq 0$. The imaginary part of lambda depends on CKM parameters only, which allows for very precise predictions.

1.4 Hadronic B Decays

A neutral B meson consists of a $\bar{\mathrm{b}}$-quark and a d- or s-quark. When it decays, the $\bar{\mathrm{b}}$-quark can only produce a $\bar{\mathrm{c}}$- or $\bar{\mathrm{u}}$-quark with an additional quark (or lepton) pair (see Figure 1.3). When this happens, the energies released are much larger than the typical quark binding energies, which lead us to the assumption that the $\bar{\mathrm{b}}$-quark decays independently of the lighter d- or s-quark. The lighter quark is hence called a spectator quark (because it does not partake in the interaction), and the assumption is called the *spectator picture*.

In the simplest case, the b-quark decay is mediated by a single virtual W boson. In addition, the exchange of gluons and other QCD effects has to be taken into account.

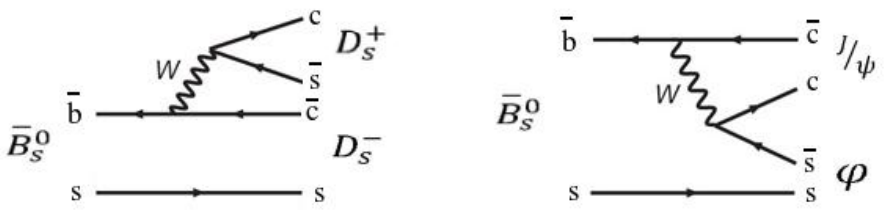

Figure 1.3: Feynman diagrams of two B meson decays, where the b-quark decays independently of the so-called spectator quark. The left diagram shows a colour-allowed tree, while the right diagram depicts a colour-suppressed tree. Both decays are mediated by a virtual W boson.

The effective Hamiltonian after gluon exchange can be expressed in terms of local four-quark operators, $O_i(\mu)$, and perturbatively calculable, scale dependent Wilson coefficients [23], $c_i(\mu)$[11]:

$$H^{eff} = \frac{G_F}{\sqrt{2}} V_{cb}^* V_{cs} \left(c_1(\mu) O_1(\mu) + c_2(\mu) O_2(\mu) \right) \ . \tag{1.26}$$

The Wilson coefficients carry all the information about the short-distance (high-energy) contributions, while the operators describes the long-range (low-energy) QCD effects. The scale, μ, is approximately m_B for B decays.

In the case of $\bar{b} \to \bar{c}c\bar{s}$ the operators are [23, 24]

$$\begin{aligned} O_1 &= (\bar{c}_i \gamma_\mu (1-\gamma_5) b_i) \, (\bar{s}_j \gamma_\mu (1-\gamma_5) c_j) \\ O_2 &= (\bar{c}_i \gamma_\mu (1-\gamma_5) b_j) \, (\bar{s}_j \gamma_\mu (1-\gamma_5) c_i) \end{aligned} \ , \tag{1.27}$$

where the indices, i and j, represent the colour of the quarks participating in the process. The only difference between the two operators is the combination of these indices.

Since mesons are colour neutral, there are only two first-order types of topologies available when a neutral B meson decays into two mesons. The first type of decay, type-I decays, are characterized by two charged mesons in the final state. In this type of decay, the W boson produces one meson, while the other meson consists of the transformed b-quark and the spectator quark. The first diagram in Figure 1.3 shows an example of a type-I decay. Here the colour combination of the produced D_s^+ meson can be chosen arbitrarily, and the diagram is hence labeled *colour-allowed*.

In the second type of decay, type-II decays, the quarks produced by the W boson are separated; one combines with the transformed b-quark, the other with the spectator quark. The latter diagram in Figure 1.3 is an example of a type-II decay. Here the final state mesons are both neutral, and the colours of their quarks are predetermined by the colours of the B meson constituents. The result is that this type of decay topology

[11] Higher order corrections can be added to the effective Hamiltonian later. When this is done, B decays into mesons should be well described by this approximation.

is suppressed by a factor $1/\mathrm{N}_C$, where $\mathrm{N}_C = 3$ is the number of available colours. A type-II decay is therefore also called a colour-suppressed decay.

Looking back at Equation 1.27, O_1 describes a colour-allowed decay, where the quarks carry matching colour indices, and O_2 describes a colour-suppressed decay. If not for the strong interaction we would have $c_1 = 1$ and $c_2 = 0$ for type-I decays, and vice versa for type-II decays.

A third type of decay arises when both types of decay topologies are available for a given final state. In this case we will have interference between the two topologies, and the operators become more complicated.

1.5 $B_s^0 \to J/\psi\,\phi$ in the Transversity Basis

$B_s^0 \to J/\psi\,\phi$ is a vector-vector decay[12] and is characterized by three angles. These angles are for convenience defined in the so-called *transversity basis*, with J/ψ decaying to two muons and ϕ to two K mesons. The advantage of working in the transversity frame is that we can define three decay amplitudes, A_0, $\mathrm{A}_\perp$ and $\mathrm{A}_\parallel$ that correspond to S-, P- and D-wave transitions respectively [25]. A_0 and $\mathrm{A}_\parallel$ are CP even, while $\mathrm{A}_\perp$ is CP odd. The separation of CP even and CP odd components of $B_s \to J/\psi\phi$ makes it possible to determine the lifetime difference between the two CP eigenstates, B_s^H and B_s^L.

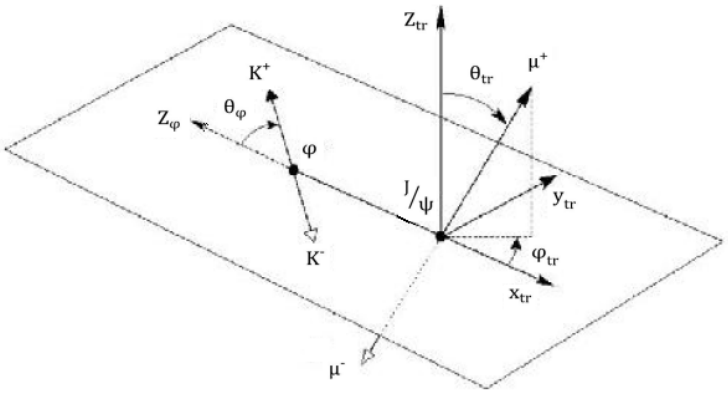

Figure 1.4: Graphical description of the transversity angles. The figure, and the below description of its parameters, are both taken from [25].

Starting in the B meson rest frame, θ_ϕ is the helicity angle of the ϕ meson, i.e. the angle between one K meson and the opposite J/ψ direction in the ϕ rest frame. θ_{tr} is the polar angle of the positively charged muon in the J/ψ rest frame defined by x_{tr}, y_{tr} and z_{tr}:
x_{tr} is the direction opposite to ϕ

[12] Both the J/ψ and the ϕ are vector mesons. A vector meson is characterized by spin-1 and negative parity.

y_{tr} is the direction perpendicular to x_{tr}, such that $p_\phi \cdot x_{tr} > 0$.
z_{tr} is the direction perpendicular to the x_{tr}-y_{tr} plane, $z_{tr} = x_{tr} \times y_{tr}$.
The last angle, ϕ_{tr} is the azimuthal angle of the positive muon, $\phi_{tr} = \arctan\left(\frac{x_{tr_{\mu^+}}}{y_{tr_{\mu^+}}}\right)$, where $x_{tr_{\mu^+}}$ ($y_{tr_{\mu^+}}$) is the x_{tr} (y_{tr}) component of the μ^+ momentum.

1.5.1 Angular Distribution

Since the amplitudes $A_0/A_\parallel$ and $A_\perp$ are related to CP-even and CP-odd states, respectively, they differ in both time evolution and angular distribution. A single-angle distribution [26],

$$\frac{d^2\Gamma}{d\cos\theta\ dt} = \frac{3}{8}\left[p(t) + 2m(t)\right] + \frac{3}{8}\left[p(t) - 2m(t)\right]\cos^2\theta\ , \tag{1.28}$$

where

$$p(t) = |A_0|^2 + |A_\parallel|^2 \quad , \quad m(t) = |A_\perp|^2\ , \tag{1.29}$$

can be employed to disentangle the CP-even and CP-odd components of the B_s, while a three-angle distribution allows one to separate out the individual amplitudes, A_0, $A_\parallel$ and $A_\perp$. In the case of $B_s \rightarrow J/\psi\phi$, the three-angle distribution for the decay of a tagged B_s meson is given by [26]

$$\begin{aligned}\frac{d^4\Gamma[B_s \rightarrow J/\psi(l^+l^-)\phi(K^+K^-)]}{d\cos\theta\ d\phi\ d\cos\psi\ dt} &= \frac{9}{32\pi}[2|A_0|^2\cos^2\psi(1-\sin^2\theta\cos^2\phi) \\ &+ \sin^2\psi\{|A_\parallel|^2(1-\sin^2\theta\sin^2\phi) + |A_\perp|^2\sin^2\theta - \mathrm{Im}(A_\parallel^* A_\perp)\sin2\theta\sin\phi\} \\ &+ \frac{1}{\sqrt{2}}\sin2\psi\{\mathrm{Re}(A_0^* A_\parallel)\sin^2\theta\sin2\phi + \mathrm{Im}(A_0^* A_\perp)\sin2\theta\cos\phi\}]\ .\end{aligned} \tag{1.30}$$

where l^+l^- can be either e^+e^- or $\mu^+\mu^-$. For $\bar{B}_s$ decays the interference terms involving $A_\perp$ are of opposite sign and all other components are unchanged.

A similar expression exists for the decay of of an untagged B_s meson. The time dependence of the untagged rate does not depend on the mass difference of the two CP eigenstates, $(\Delta m)_{B_s}$ (as shown in [27]). Consequently, Γ_L and Γ_H can be determined from data sample of untagged B_s mesons, while the extraction of $(\Delta m)_{B_s}$ requires tagging (see [27]).

It is the separation of Γ_L and Γ_H, and consequently, the determination of the lifetime difference between CP-even (B_s^L) and CP-odd (B_s^H) states, that we ultimately would like to study in ATLAS.

Chapter 2

The ATLAS Experiment

Particles are detected via their interactions with matter. For many years the bubble chamber was the major experimental tool, but when Georges Charpak, in 1968, developed the multiwire proportional chamber, particle detection passed from the manual to the electronic era [28]. The digitized recording of experimental data, enabled faster processing and larger amounts of data to be analyzed.

In this chapter I will describe the machinery used to produce and detect data. The accelerator complex will only be mentioned briefly, while the technical details and performance of the different sub-systems of the ATLAS detector will be mentioned in more detail. All facts, numbers and figures in Section 2.2 are taken from reference [29] unless stated otherwise.

2.1 CERN and the LHC

CERN (European Organization for Nuclear Research)[1] is the worlds largest scientific laboratory dedicated to fundamental research. It is located near Geneva, Switzerland, on the French-Swiss border. Since the start-up in 1954, the number of member states has almost doubled, from the initial 12 to the 20 it is today.

Several experiments are currently taking place at CERN, but the main focus is on the start-up of the Large Hadron Collider (LHC) [30] and on the four main experiments connected to it. The LHC is a synchrotron storage ring, located about 100 m below ground (varying from approximately 175 m under the Jura mountains, to about 50 m towards Lake Geneva). It is the largest of its kind, with a circumference of approximately 27 km. The LHC will accelerate protons to a center of mass (cm) energy of up to 14 TeV, and provide collisions at four points along the ring (point 1, 2, 5 and 8) where the four major

[1] The name CERN was originally an acronym for the French Conseil Européen pour la Recherche Nucléaire, or European Council for Nuclear Research. The council existed as a prelude to the CERN we know today, and was dissolved when the organization officially came into being in 1954. It was then given the name Organisation Européen pour la Recherche Nucléaire, or European Organization for Nuclear Research. The acronym however, was retained [28].

experiments are located. These are ATLAS, CMS, LHCb and ALICE. Figure 2.1 shows a drawing of the underground accelerator, indicating where the different experiments are located.

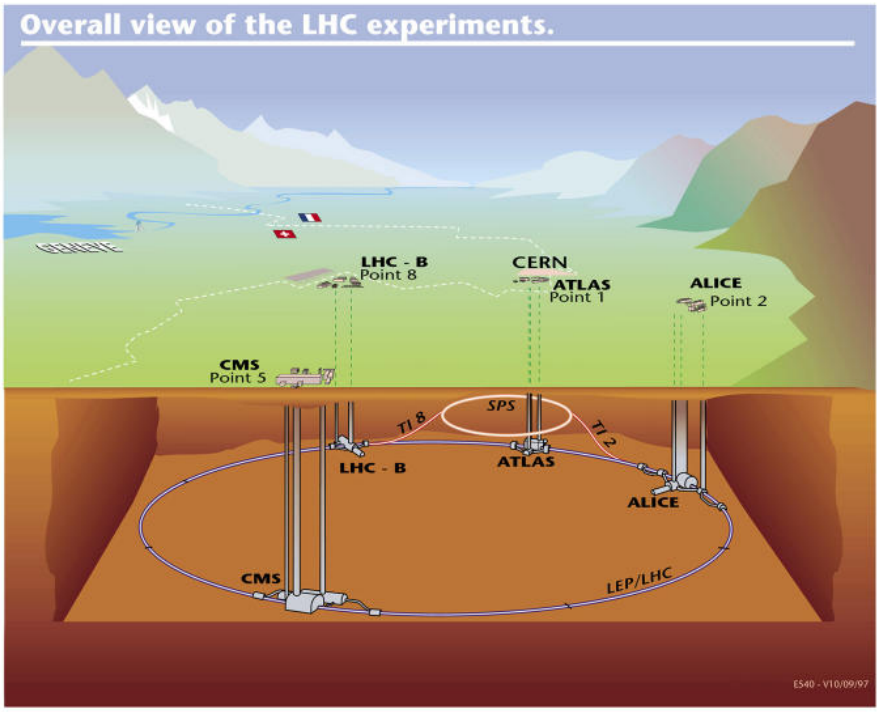

Figure 2.1: The LHC accelerator, spanning the borders of France and Switzerland, will provide collisions at four different points, where the main experiments are located.

During shorter periods of time, the LHC will also provide heavy-ion collisions (A-A collisions). However, since my analysis solely focuses on the physics of proton-proton (p-p) collisions, heavy ion collisions will not be covered here.

The two proton beams will be kept in orbit by a chain of steering and focusing magnets. Each magnet structure contains two separate bores (one for each beam), located within a shared vacuum pipe as shown in Figure 2.2. To achieve the desired magnetic field to keep the protons in the ring, the magnets are cooled down to as low as 1.9 K, making them superconducting[2]. The number of events per second generated in the LHC collisions is given by

$$N_{event} = \mathscr{L}\sigma_{event} \,, \tag{2.1}$$

where $\mathscr{L}$ the machine luminosity and σ_{event} is the cross-section for the event under study. The machine luminosity depends only on the beam parameters and can be expressed as [32]

$$\mathscr{L} = \frac{N_b^2 n_b f_{rev}}{A} \,, \tag{2.2}$$

[2] The LHC beam-structure is the largest superconducting installation in the world.

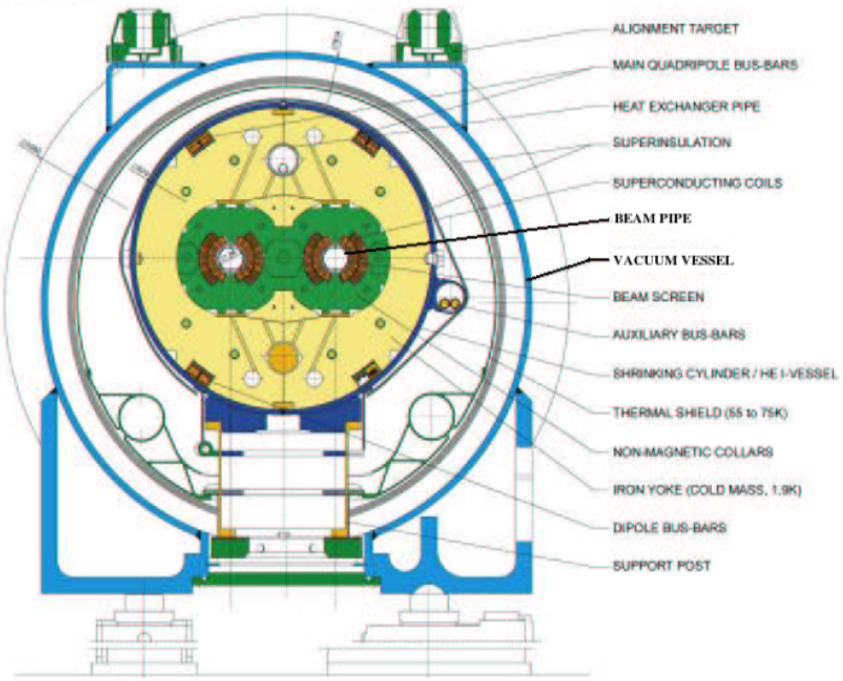

Figure 2.2: Cross-section of the LHC dipole magnet [31]. In the center we see the two bores that will house the proton beams.

where N_b is the number of particles per bunch, n_b the number of bunches per beam, f_{rev} the revolution frequency and A the beam cross-section area, which is given by $4\pi\sigma_x\sigma_y$, where σ_x and σ_y are the beam sizes in the horizontal and vertical directions respectively.

Another much used quantity is the integrated luminosity, L, expressed as

$$L = \int \mathscr{L}\, dt\ . \tag{2.3}$$

When the design luminosity of 10^{34} cm^{-2}s^{-1} is reached, one expects an integrated luminosity of around 100 fb^{-1} per year.

2.1.1 The LHC Injection Chain

When the LHC starts running, it will accelerate protons to a nominal energy of 7 TeV. The protons will be injected into the LHC in bunches, with about 10^{11} protons per bunch and 2808 bunches per beam [30]. This translates into a nominal bunch spacing of 25 ns. When the bunches are brought together, about 20 p-p collisions will take place, producing a large amount of data for the detectors to analyze.

Before being injected into the LHC ring, the protons pass through a set of pre-accelerators. The full injection chain is shown in Figure 2.3. First the protons are pro-

duced by stripping electrons from hydrogen atoms. They are then accelerated to 50 MeV by the Linear Accelerator (Linac2), before being injected into the Proton Synchrotron Booster (PSB), a synchrotron made up of four superposed rings [31]. Here the protons are given an energy of 1.4 GeV, before they are passed on, this time to the Proton Synchrotron (PS). The PS was one of CERN's first two accelerators (completed in 1959). It has a circumference of 628 m and runs at a proton beam energy of approximately 25 GeV. The protons for the LHC are extracted from the PS and put into the Super Proton Synchrotron (SPS), which is the machine used when the first discovery of the W and Z boson were made in 1983, and when direct CP violation was observed in 2001 [31]. Here the protons are accelerated to 450 GeV before they are finally injected into the LHC and accelerated to the desired energy of 7 TeV. (All energies in this section are taken from [30].)

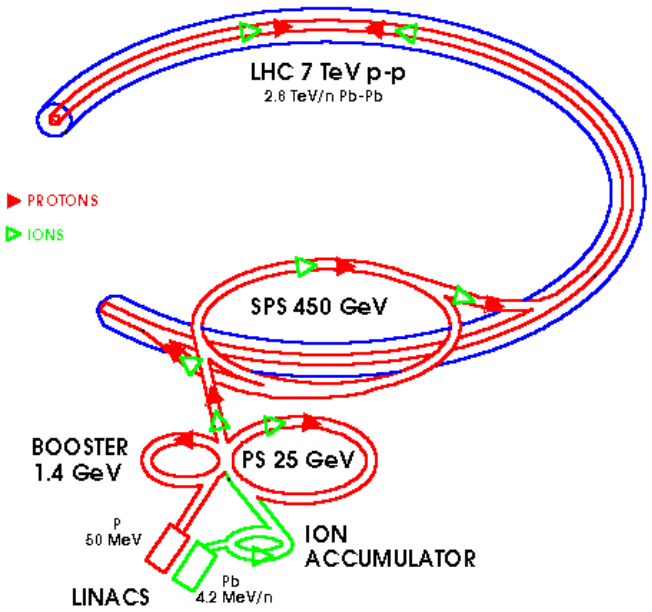

Figure 2.3: The LHC injection chain: Linac2 – PSB – PS – SPS – LHC. The figure is taken from [30].

2.2 The ATLAS Detector

ATLAS (A Toroidal LHC ApparatuS) is one of four major experiments at the LHC. The three others are CMS (Compact Muon Solenoid), ALICE (A Large Ion Collider Experiment) and LHCb (LHC-beauty). The two latter are dedicated heavy ion and b-physics

experiments respectively, while CMS and ATLAS are general purpose detectors, meaning that a broad spectrum of physics studies will be performed by these experiments.

Figure 2.4 shows the layout of the ATLAS detector. It has a cylindrical geometry, is approximately 42 meters long, and has a radius of about 11 meters. The whole detector weighs about 7000 tonnes. Mechanically it is divided into three parts; the barrel in the middle region, and two end-caps at either side of the barrel. These are mainly made up of the four major sub-detector systems; the inner detector, the calorimeters, the muon detectors and the magnet systems. The inner detector is located closest to the interaction point and provides the highest granularity measurements. It is essential, amongst other things, for B-tagging, reconstruction of secondary vertices, and in obtaining high resolution momentum measurements. Enveloping the inner detector are the calorimeters, which are responsible for providing high accuracy energy measurements and distinguishing the hadrons from the electrons and photons in the detector. The muons are identified by the muon spectrometer, which makes up the outermost parts of the ATLAS detector. The main task of the muon spectrometer is measuring the muon momenta, in addition to providing an efficient muon trigger system. The magnet system works in conjunction with the three other sub-systems. It provides high magnetic fields, which is necessary to determine the particle momenta. In this section I will describe the technical details of these four sub-systems. I will also briefly discuss the ATLAS trigger and data acquisition systems.

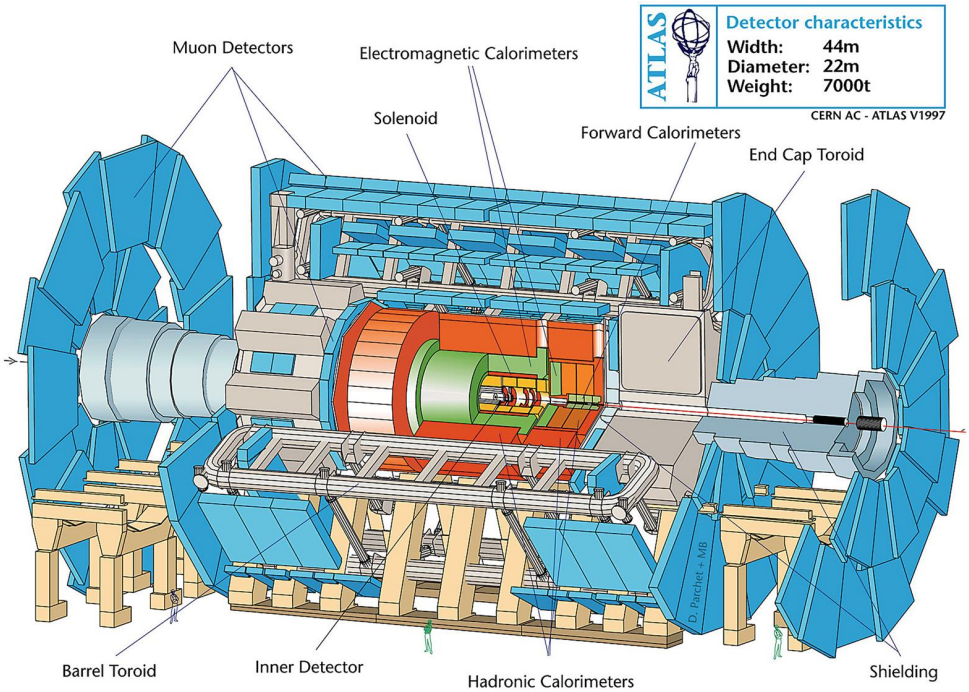

Figure 2.4: Overall layout of the ATLAS detector [33].

2.2.1 Geometry

In order to describe what we see in the ATLAS detector, we define a common (right-handed) coordinate system [34], where the z-axis is given by the beam direction. The x-y plane is the plane perpendicular to the beam, with the positive x-axis pointing from the Interaction Point (IP) towards the center of the LHC ring, and the positive y-axis pointing upwards. The azimuthal angle, ϕ, is defined as

$$\phi \equiv \tan^{-1}\left(\frac{p_y}{p_x}\right) ,$$

where p_x (p_y) is the x-component (y-component) of the particle momentum. The pseudorapidity is defined as

$$\eta = -\ln\left(\tan\left(\frac{\theta}{2}\right)\right) ,$$

where θ is the polar angle, i.e. the angle from the beam axis. For relativistic, light particles the pseudorapidity is a good approximation to the rapidity:

$$y = \frac{1}{2}\ln\left(\frac{E + p_L}{E - p_L}\right) ,$$

where E is the particle's energy and p_L is its momentum parallel to the beam axis. In a large collider experiment like ATLAS one may not always have the ability (or the time) to compute a particle's longitudinal momentum (and energy), making the pseudorapidity the preferable variable. It behaves like the rapidity, giving it the same advantages with respect to just using the polar angle: It is independent of the Lorentz boost along the beam axis, and the particle production is approximately constant as a function of the (pseudo)rapidity [35].

The transverse variables, e.g. the transverse momentum p_T, lie in the x-y plane. The distance ΔR in the η-ϕ plane is defined as

$$\Delta R = \sqrt{\Delta\eta^2 + \Delta\phi^2} .$$

Simply put, it is the quantity used to describe the distance between the direction of two objects, i.e. two particles, in the detector [34].

The transverse impact parameter, d_0, is defined as the transverse distance between the beam axis and the point of closest approach. It is proportional to the flight distance of a particle, which is useful when calculating the particle's lifetime.

2.2.2 The Inner Detector

At the center of ATLAS lies the Inner Detector (ID). It provides high granularity measurements over the range $|\eta| < 2.5$. Among its main responsibilities are B-tagging, reconstruction of secondary vertices from b- and τ-decays, and identification of the primary vertex. It also needs to provide a high track finding efficiency and an excellent

momentum and impact parameter resolution for tracks with $p_t > 0.5$ GeV up to very high momentum.

The ID is approximately 6.2 meters long and has a diameter of about 2.1 meters. It consists of three independent but complementary sub-detectors as shown in Figure 2.5. The silicon pixel detector is located closest to the interaction point because it provides the highest granularity. The SemiConductor Tracker (SCT) is made up of silicon microstrips, and is situated around the pixel detector. In the barrel region the pixels and strips are located on concentric cylinders around the beam-pipe while in the end-cap regions they are placed on discs perpendicular to the beam axis. The final sub-system of the ID is the Transition Radiation Tracker (TRT). This consists of straw tubes that are arranged parallel to the beam axis in the barrel region and radially in wheels in the end-cap regions. Figure 2.5 shows the layout of the inner detector.

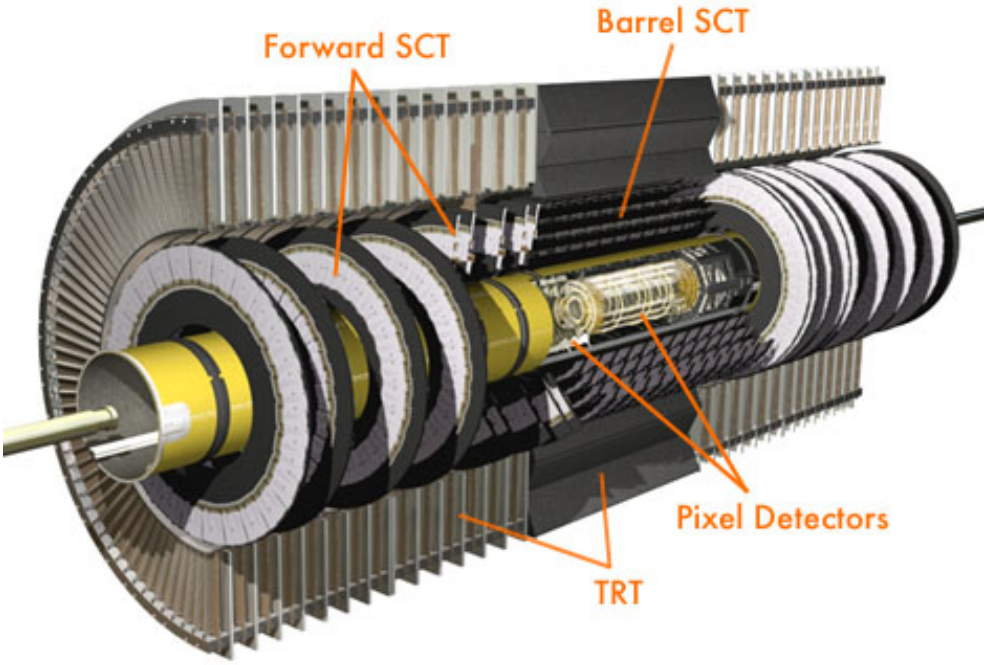

Figure 2.5: Cut-away view of the ATLAS inner detector [36].

The Pixel Detector

All the 1744 pixel sensors are identical, with external dimensions 19 $\times$ 63 mm^2. Each contains more than 46000 pixel elements of minimum 50 $\times$ 400 μm^2. They are arranged in three cylindrical layers in the barrel with three end-cap disks on either side. The innermost barrel layer will later be referred to as the b layer. Figure 2.6 shows the position of the layers and disks relative to the interaction point. The spacing between the layers and disks are such that most tracks will typically give three hits when passing through the pixel detector. The intrinsic resolutions are 10 μm (R–ϕ) and 115 μm (z) in

the barrel, and 10 μm (R–ϕ) and 115 μm (R) in the disks. About 80.4 million channels are read out.

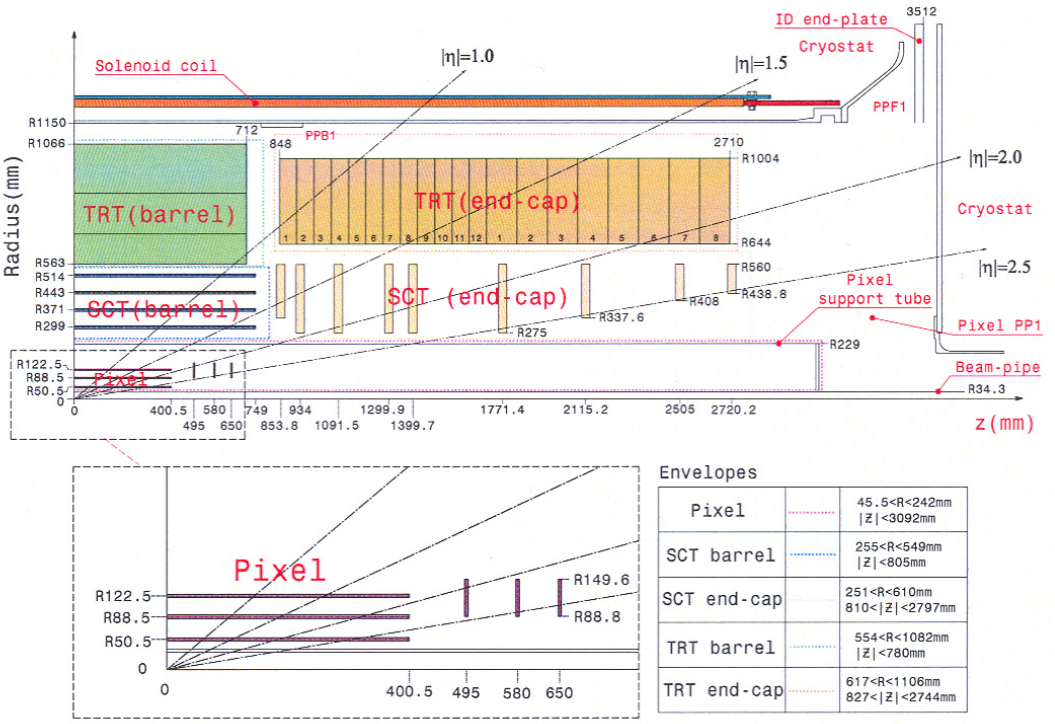

Figure 2.6: Plan view of a quarter-section of the ID showing the position of each of the major detector elements.

The SCT

The SCT consists of 4088 modules, distributed between the barrel and end-caps. The silicon microstrips of the SCT barrel are arranged in four double layers (see Figure 2.6 for the exact positions in R–z). One of the strips in each layer is parallel to the beam axis while the other is at a 40 mrad angle, making it possible to measure both R–ϕ and z. In the end-caps there are nine disks of back-to-back strips. Here one set of strips are running radially while the other is at a 40 mrad angle. The intrinsic resolutions per module are 17 μm (R–ϕ) and 580 μm (z) in the barrel, and 17 μm (R–ϕ) and 580 μm (R) in the disks. A total of approximately 6.3 million channels are read out.

Both the pixels and the SCT cover the range $|\eta| < 2.5$.

The TRT

The TRT consists of 136 modules of straw tubes interleaved with transition radiation material, which is important for electron identification. Each tube has a diameter of 4 mm and a length of 144 cm (barrel) or 37 cm (end-cap). They contain a gas mixture of 70 % Xe, 27 % CO_2 and 3 % O_2. In the barrel region the straws are arranged in three layers and are parallel to the beam axis, with their anode wires divided into two equal parts. In the end-cap regions they are arranged radially in wheels. Figure 2.6 shows the position of the TRT with respect to the IP.

Unlike the pixel and SCT detectors, the TRT only gives a measurement in R – ϕ, and it covers the slightly smaller region up to $|\eta|$ = 2.0. However, due to the large number of hits per track (typically 36), the TRT contributes significantly to the momentum measurements of the detector. A total of about 351,000 channels are read out, and the intrinsic resolution per straw is 130 μm.

Inner Detector Tests

In addition to simulation tests of the inner detector, its components have been tested separately, in combined test-beam (CTB) exercises, and with cosmics. The resolutions of separate channels, as well as the tracking performance after alignment are all in agreement with the design specifications. Figure 2.7 shows the resolution for the radial position of the secondary vertex for $J/\psi \rightarrow \mu\mu$ decays in events containing B-hadrons, as a function of the pseudorapidity of the J/ψ, as obtained from simulated data, while Figure 2.9 shows an example of a graphical display of one of the cosmic muon events taken this spring.

2.2.3 The Calorimeters

The ID is surrounded by the Central Solenoid (CS) magnet (described in Section 2.2.5), which again is enveloped by an electromagnetic and a hadronic calorimeter. Their main task is to provide high accuracy energy measurements of the particles traversing the detector. Photons and electrons will produce showers in the electromagnetic calorimeter, while hadrons (both charged and neutral) will produce showers in the hadronic calorimeter. Figure 2.10 shows the calorimeters convoluting the inner detector and central solenoid magnet. The brown parts show the LAr (Liquid Argon) electromagnetic calorimeter while the grey and copper parts make up the hadronic calorimeter. All calorimeters in ATLAS are sampling calorimeters, meaning that they consist of alternating layers of active and passive material. It is only the energy of the active layers that is collected.

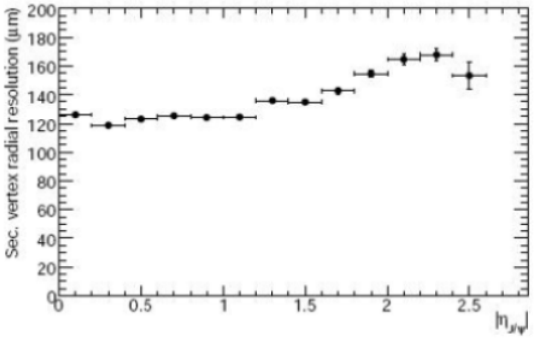

Figure 2.7: Secondary vertex radial position resolution as a function of pseudorapidity for $J/\psi \rightarrow \mu\mu$ from B-hadron decays. The J/ψ have an average transverse momentum of 15 GeV.

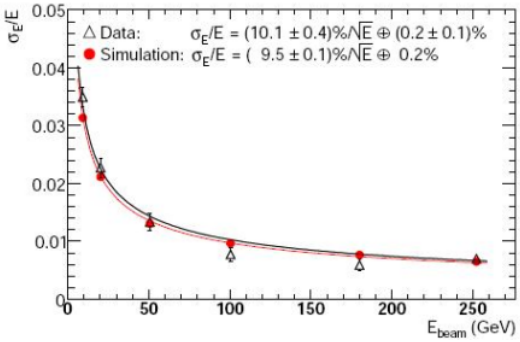

Figure 2.8: Relative energy resolution as a function of the electron beam energy, for a barrel LAr electromagnetic module in the combined test-beam. Electronic noise has been subtracted from the data. The results are shown for an amount of upstream material of 2.4 radiation lengths, which is that expected in ATLAS at $\eta = 0.4$. The curve is described by function 2.4.

The Electromagnetic Calorimeter

The EM calorimeter is a lead-LAr calorimeter, with accordion-shaped kapton electrodes and lead absorber plates over its full coverage. The barrel is divided into two identical halves, separated by a small gap, of approximately 4 mm, at z $= 0$. It covers the region $|\eta| < 1.475$, while the end-caps cover the region $1.375 < |\eta| < 3.2$. The end-caps are divided into two coaxial wheels: the outer wheel ($1.375 < |\eta| < 2.5$) and the inner wheel ($2.5 < |\eta| < 3.2$). This geometry provides a complete ϕ symmetry without any azimuthal cracks. The thickness of the lead absorber plates has been optimised as a function of η to provide the best possible resolution when measuring the energy deposited in the calorimeter.

In the region of $|\eta| < 1.8$, a presampler detector is introduced between the cryostat and CS to correct for the energy lost by electrons and photons before reaching the calorimeter. It consists of an active LAr layer of thickness 1.1 cm (0.5 cm) in the barrel (end-cap) region.

Four barrel and three end-cap modules have been tested with electron and positron beams of energies between 1 and 250 GeV. In addition, a spare electromagnetic barrel module was built for a combined test-beam period in 2004. It was exposed to electron, photon, pion and muon beams with energies between 1 and 350 GeV. The measured relative energy resolutions and position resolutions were all within what was expected from the detector description and from simulations of the test-beam setup. The relative

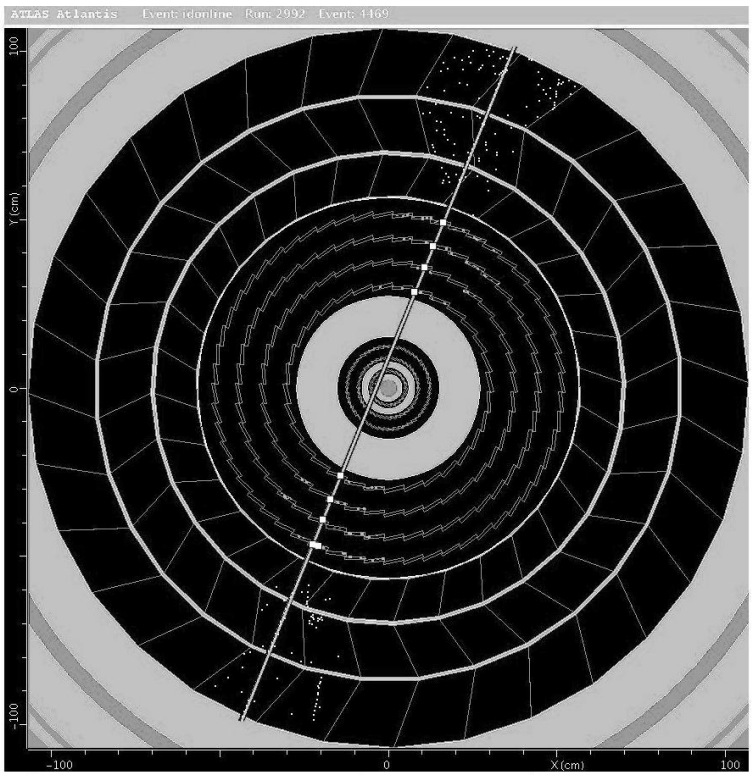

Figure 2.9: A cross-section of the barrel SCT and TRT during a cosmic muon event. The hits (white dots in TRT, white squares in SCT) have been fitted to a straight line (the muon track). The dots surrounding the line are due to noise in the active detector parts.

energy resolution is parametrized by:

$$\frac{\sigma(E)}{E} = \frac{a}{\sqrt{E(GeV)}} \oplus b \,, \tag{2.4}$$

where a is a stochastic term and b is a constant term reflecting local non-uniformities in the response of the calorimeter. The symbol, $\oplus$, indicates summation in quadrature. Figure 2.8 shows a plot of the relative energy resolution as a function of the beam energy, measured during test-beam runs. The position resolution along η was measured in a stand-alone test [37] and found to be of the order of 10^{-4} (in units of pseudorapidity) at 245 GeV, allowing to achieve a polar angle resolution in the range 50–60 mrad/$\sqrt{E}$ (GeV) for both barrel and end-caps.

The Hadronic Calorimeters

The hadronic calorimeter is located directly outside the electromagnetic calorimeter, and consists of three sub-systems: **The tile calorimeter** is divided into a barrel part ($|\eta| < 1.0$) and an extended barrel part ($0.8 < |\eta| < 1.7$) on either side. It is a sampling

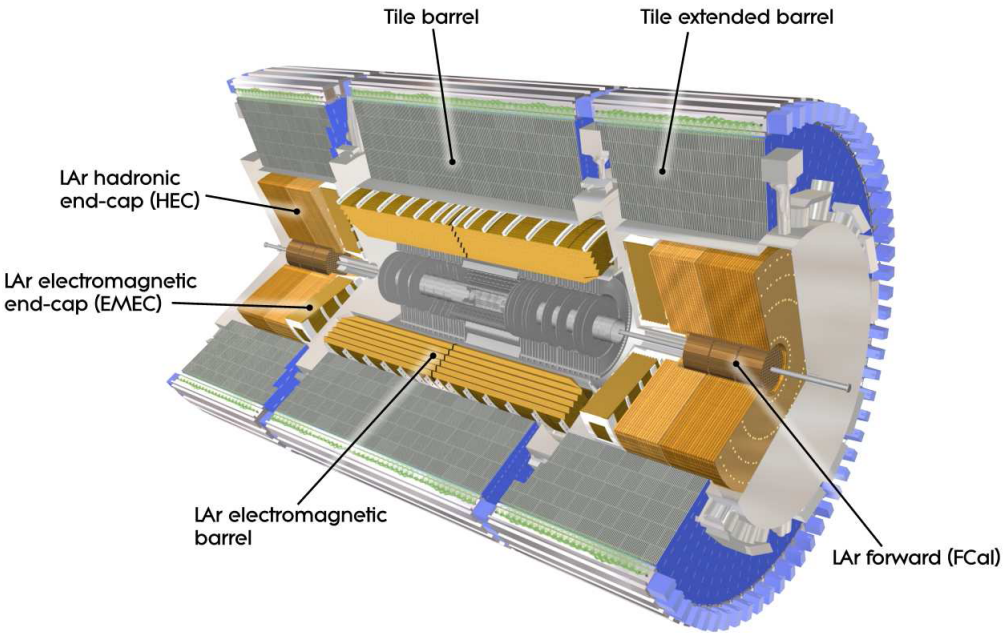

Figure 2.10: The calorimeters.

calorimeter with steel absorbers, and plastic scintillating tiles as the active material. The scintillating tiles are 3 mm thick while the steel absorbers consist of a 5 mm thick master plate, onto which 4 mm thick spacer plates are glued in a staggering fashion to form the pockets in which the scintillator tiles are located. Both the barrel and extended barrels are divided azimuthally into 64 wedges to simplify the detector construction. **The LAr end-cap calorimeter** consists of two independent wheels per end-cap, where each wheel is made up of 32 identical wedge-shaped modules. The wheels closest to the IP consist of 25 mm copper plates interleaved with 8.5 mm LAr gaps. Those further away use 50 mm copper plates. Also these are interleaved with 8.5 mm LAr gaps. To reduce gaps at the transition between the end-cap and the forward calorimeter the hadronic end-cap calorimeter is extended so that the two calorimeters overlap slightly (see Figure 2.10). **The forward calorimeter** consist of three modules in each end-cap. The first, made of copper, is optimised for electromagnetic measurements, while the other two, made of tungsten, measure predominantly the energy of hadronic interactions. All three use LAr as the active material.

In order to reduce the amount of neutrons in the inner detector cavity due to reflection off the front face of the forward calorimeter, the latter is recessed by about 1.2 m with respect to the EM calorimeter front face.

The hadronic calorimeters have also gone through extensive testing. Figure 2.11 shows the relative energy resolutions of the forward calorimeter measured with pion beams

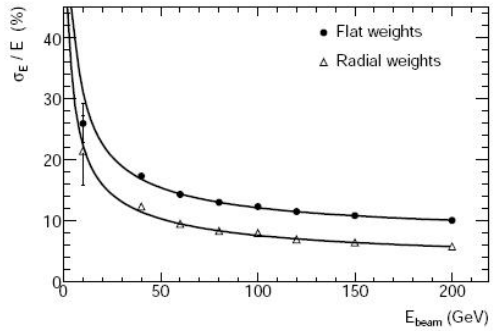

Figure 2.11: Relative energy resolution obtained for pions, measured in all three modules of the forward calorimeter, as a function of the beam energy. The data points correspond to two different cell-weighting schemes, and the curves correspond to the result of a fit to the data points using equation 2.4.

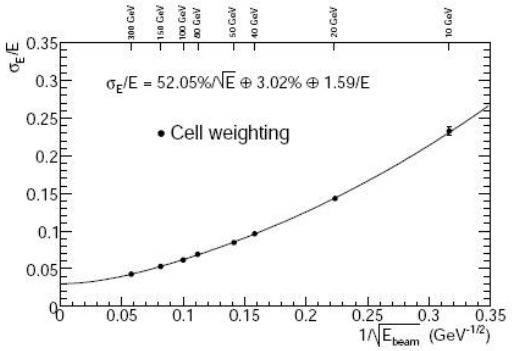

Figure 2.12: Relative energy resolution obtained for pions as a function of the inverse square root of the beam energy, for combined LAr and tile calorimeter at $|\eta|$ =0.25. The curve corresponds to the result of a fit to the data points with the functional form as shown.

of momenta between 10 and 200 GeV, while Figure 2.12 shows the relative energy resolution for the combined LAr and tile calorimeter. The measured resolutions are well within the design specifications.

2.2.4 The Muon Spectrometer

The conceptual layout of the muon spectrometer is shown in Figure 2.13, while a cross-section of the barrel part is depicted in Figure 2.14. In the barrel region the chambers are arranged in three concentric cylindrical layers around the beam axis (at radii of approximately 5 m, 7.5 m, and 10 m), while in the end-cap regions the chambers are arranged to form large wheels perpendicular to the beam axis (at $|z| \approx 7.4$ m, 10.8 m, 14 m, and 21.5 m).

The muon spectrometer is the largest sub-system of the ATLAS detector, and its main task is to measure the momenta of muons in the pseudorapidity range $|\eta| < 2.7$. In addition it is responsible for triggering on these muons in the region $|\eta| < 2.4$. To accomplish this with adequate precision, four different chamber technologies have been employed. The precision momentum measurement is mainly performed by the Monitored Drift Tube chambers (MDTs). These cover the pseudorapidity range $|\eta| < 2.7$ (except in the innermost end-cap layer where their coverage is limited to $|\eta| < 2.0$). They consist of three to eight layers of drift tubes, with the layer dimensions and chamber sizes increasing in proportion of their distance to the interaction point. An average position resolution of about 35 μm per chamber is achieved. In the forward region ($2.0 < |\eta| < 2.7$), Cathode-Strip Chambers (CSCs) are used in the innermost layer due to their superior rate capability and time resolution. The CSCs are multiwire proportional chambers

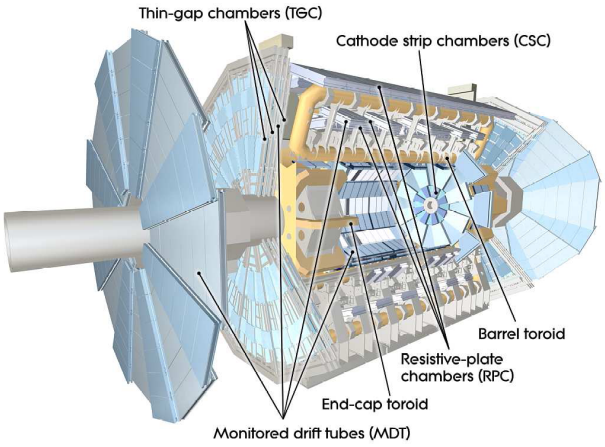

Figure 2.13: Cut-away view of the ATLAS muon system, indicating where the different chamber technologies are used.

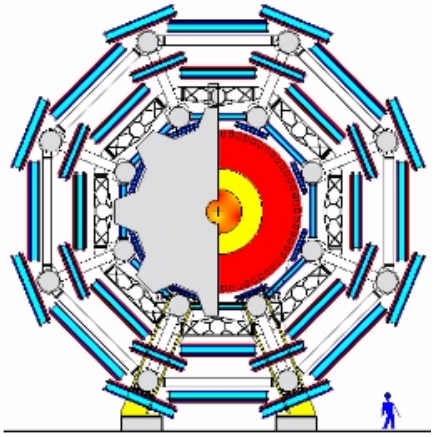

Figure 2.14: Cross-section of the barrel muon system perpendicular to the beam axis [38], clearly exhibiting the three radial layers of chambers.

with cathode planes segmented into strips in orthogonal directions, which allows for measurements of both spatial coordinates. The resolution of a chamber is about 40 μm in the bending (η) plane and about 5 mm in the transverse (ϕ) plane (Table 2.1).

In addition to measuring the muon momenta, the muon spectrometer also needs to be able to trigger on muon tracks. This is achieved by introducing a system of fast trigger chambers in addition to the MDTs and CSCs. The trigger chambers have three main responsibilities: i) Provide bunch-crossing identification, ii) yield well defined p_T thresholds, and iii) measure the muon coordinate in the direction orthogonal to that determined by the precision-tracking chambers. Hence, the trigger chambers need to measure both track coordinates, and be capable of delivering track information within a few tens of nanoseconds after the passage of a particle. In the barrel region ($|\eta| <$

		Chamber resolution (RMS) in			**Measurements per track**	
Type	**Function**	z/R	ϕ	time	barrel	end-cap
MDT	tracking	35 μm (z)	–	–	20	20
CSC	tracking	40 μm (R)	5 mm	7 ns	–	4
RPC	trigger	10 mm (z)	10 mm	1.5 ns	6	–
TGC	trigger	2-6 mm (R)	3-7 mm	4 ns	–	9

Table 2.1: Main parameters of the four sub-systems of the muon detector. Column 5 lists the intrinsic time resolution of each chamber type, to which contributions from signal-propagation and electronics contributions need to be added. The table is a modification of a table in [29].

1.05), Resistive Plate Chambers (RPCs) were selected for this purpose, while in the end-cap ($1.05 < |\eta| < 2.4$) Thin Gap Chambers (TGCs) were chosen. The RPCs are gaseous parallel electrode-plate detectors. The parallel resistive plates are separated by 2 mm, and the volume between them contains a gas mixture of $C_2H_2F_4$/Iso-C_4H_{10}/SF_6 (94.7%/5%/0.3%). An electric field between the plates of about 4.9 kV/mm allows avalanches to form along the ionising tracks towards the anode. Figure 2.15 shows a standard barrel sector and the location of the RPCs (coloured) relative to the MDTs. The large lever arm between inner and outer RPCs allows the trigger to select high momentum tracks in the range 9–35 GeV, while the two inner chambers provide the low-p_t trigger in the range 6–9 GeV. All three chambers consist of two independent detector layers.

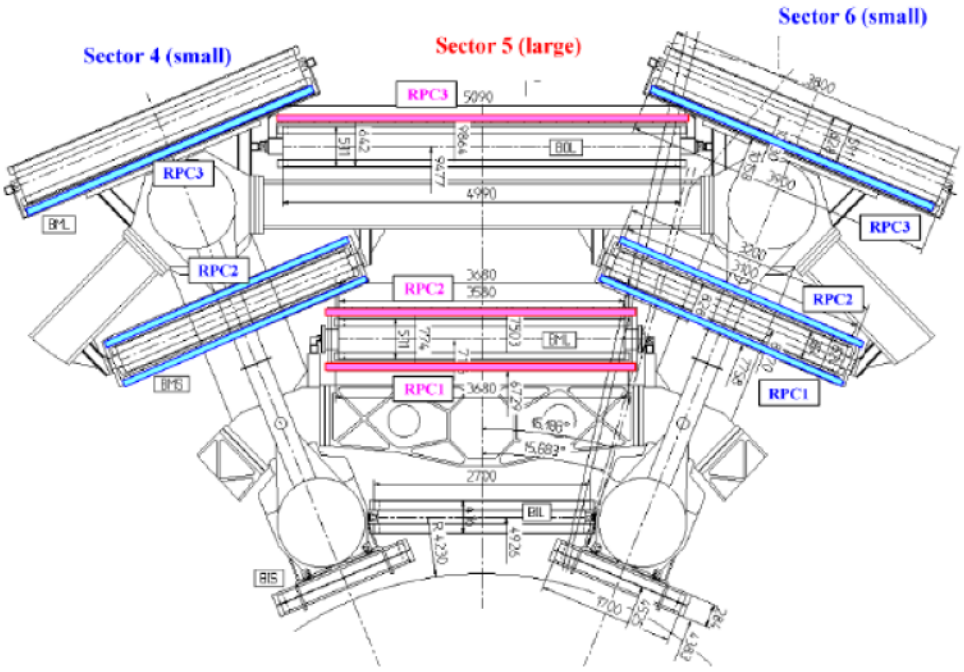

Figure 2.15: Cross-section through the upper part of the barrel with the RPCs marked in colour. In the middle chamber layer, RPC1 and RPC2 are below and above their respective MDT partner. In the outer layer, the RPC3 is above the MDT in the large and below the MDT in the small sectors. All dimensions are in mm.

The middle layer of the MDTs in the end-cap is complemented by seven layers of TGCs, while the inner layer is complemented by only two layers. The TGCs are multiwire proportional chambers with the characteristic that the wire-to-cathode distance of 1.4 mm is smaller than the wire-to-wire distance of 1.8 mm. The chambers are filled with a highly quenching gas mixture of CO_2 and n-C_5H_{12}, and the small wire-to-wire distance combined with a high electric field around the TGC wires lead to a very good

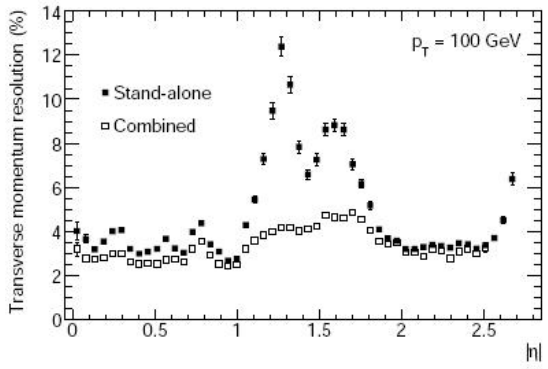

Figure 2.16: Expected transverse momentum resolution as a function of η. Solid data points are shown for tracks measured in the muon system alone (stand-alone reconstruction) and open points for tracks measured in both the inner detector and muon systems (combined reconstruction).

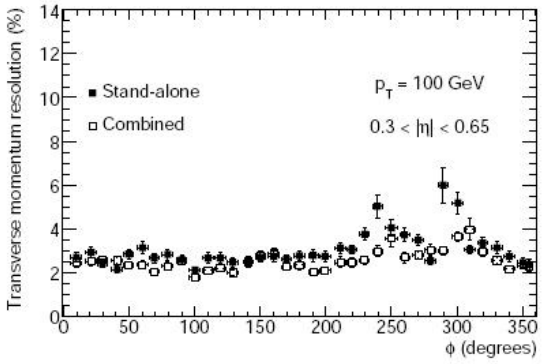

Figure 2.17: Expected transverse momentum resolution as a function of ϕ for stand-alone and combined reconstruction.

time resolution for most of the tracks. Table 2.1 summarizes the different chamber properties.

When installing the muon chambers in the ATLAS pit, proper alignment is an important issue. Most chambers therefore use an optical alignment system. The accuracy of this system has been tested during test-beam periods, and accuracies of approximately 20 μm have been achieved (which is well within the design specifications). The performance of the chambers have also been thoroughly tested. As an example, Figure 2.16 shows the momentum resolution as a function of $|\eta|$, averaged over ϕ, for single muons with $p_T = 100$ GeV, obtained for stand-alone (only using the muon spectrometers) and combined (muon spectrometer and inner detector) muon tracks. Over a large fraction of the acceptance, the stand-alone resolution is close to the combined resolution of $\sim$3%, as shown in more detail in Figure 2.17, which shows a close-up of the region $0.3 < |\eta| < 0.65$. One can clearly see the degradation in resolution close to $\phi = 240$ and 300 degrees, where the support structures for the barrel part of the detector are located.

2.2.5 The Magnet System

ATLAS has four big superconducting magnets: A Central Solenoid (CS) located in front of the EM calorimeter, and three air-core toroids (one barrel and two end-caps). Figure 2.4 shows where the magnets are located within the detector, while Figure 2.18 shows the geometry of the magnet windings in some more detail.

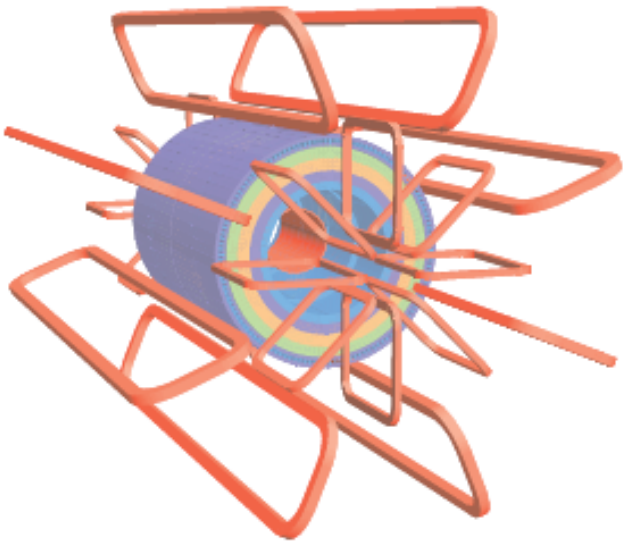

Figure 2.18: Geometry of the magnet windings and the tile calorimeter steel. The eight barrel toroid coils are visible, with the end-cap toroid coils interleaved. The solenoid windings lie inside the calorimeter volume [29].

The Central Solenoid

The CS is located between the ID and the EM calorimeter. It provides a magnetic field of 2 T, resulting in a deflection of charged particles in the transverse plane in the ID, allowing their momenta to be measured. Because of its position in front of the EM calorimeter, it is designed to be as thin as possible in order not to disturb the desired calorimeter performance

The Aircore Toroids

The three toroids provide an average magnetic field of 0.5 T and 1.0 T for the muon detectors in the central and end-cap regions, respectively. Each of the toroids consists of eight coils assembled radially and symmetrically around the beam axis (illustrated in Figure 2.18). The two end-cap toroids are inserted in the barrel toroid at each end and line up with the CS. They are also rotated by 22.5 degrees with respect to the barrel toroid coil system in order to optimise the bending power in the transition region between the two coil systems.

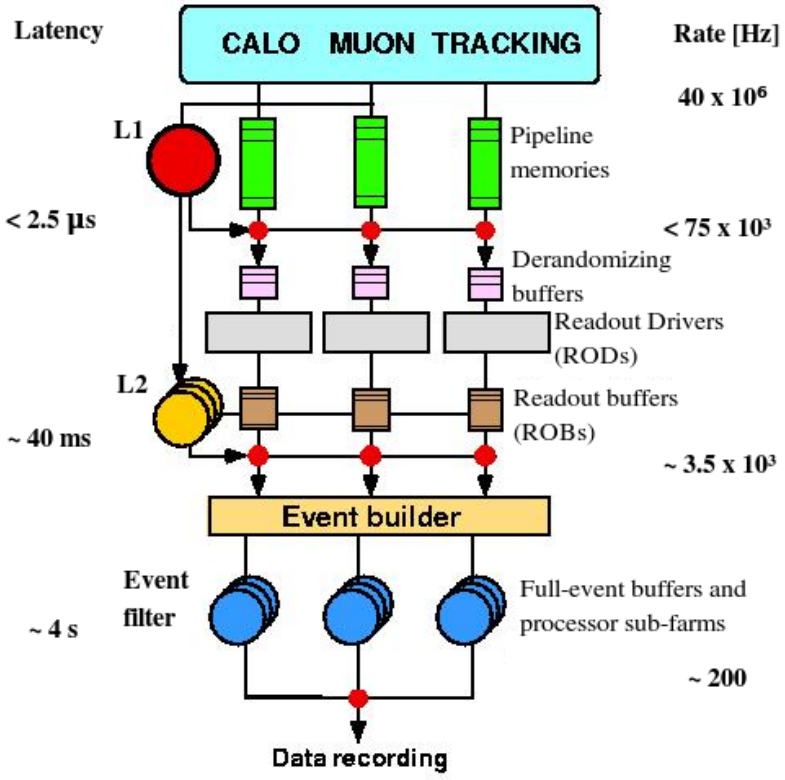

Figure 2.19: Schematic of the ATLAS trigger system, with the expected rate after each level and the latency of each step indicated.

2.2.6 Trigger and Data Acquisition Systems

At the LHC design luminosity, a bunch-crossing rate of about 40 MHz is expected. On average, every bunch-crossing will produce 23 p-p collisions, making the interaction rate close to 1 GHz. To deal with the huge amount of information, stringent requirements are put on the performance of the detectors' trigger and data aquisition systems. The data rate needs to be reduced to about 200 events per second before it can be passed on to permanent storage.

The data aquisition system (DAQ) is responsible for moving the data. In addition the DAQ also provides for the control and monitoring of the ATLAS detector during data-taking. Supervision of the detector hardware is provided by the Detector Control System (DCS) [39].

The trigger consists of three levels of on-line event selection: Level-1 (L1), Level-2 (L2), and event filter (EF). The L2 trigger and event filter together form the High-Level Trigger (HLT). Each trigger level refines the decisions made at the previous level, and applies additional selection criteria where necessary. Figure 2.19 illustrates the event reduction procedure.

Level-1 Trigger

The L1 trigger searches for signatures from high p_T muons, electrons/photons, jets, and τ-leptons decaying to hadrons. It also selects events with large missing transverse energy (E_T^{miss}) and events with large total transverse energy. Its selection is based on reduced-granularity information from a subset of detectors: Resistive Plate Chambers (RPC) and Thin-Gap Chambers (TGC) for high p_T muons, and all the calorimeter subsystems for electromagnetic clusters, jets, τ-leptons, large E_T^{miss}, and large total transverse energy. In each event the L1 trigger also defines one or more Regions Of Interest (ROI). The ROI data contain information on the type of feature identified and the criteria passed. Information about the geometric location of trigger object is retained in the muon and calorimeter trigger processers. While the trigger decision is being made, the information for all detector channels is retained in pipeline memories. The maximum L1 acceptance rate that the detector readout systems can handle is 75 kHz, and the L1 latency, i.e. the time from the initial collision until the L1 trigger decision is passed, has to be smaller than 2.5 μs.

Level-2 Trigger

After an event is accepted by the L1 trigger, the data from the pipelines are transferred off the detector to the Readout Drivers (RODs). The digitized signals are formatted as raw data before being transferred to the Data Aquisition (DAQ) system. The first stage of the DAQ, the Readout System (ROS), receives and temporarily stores the data in local Readout Buffers (ROBs). The L2 trigger then makes its selection using, at full granularity and precision, all the available data (including data from the inner detector) within the ROIs defined by the L1 trigger. It reduces the event rate to below 3.5 kHz, with an average event processing time of $\sim$ 40 ms.

Event Filter

Events selected by the L2 trigger are passed on to the event-building system and subsequently to the event filter for the final selection. The event filter stores the fully-built events and uses offline procedures to further trim the number of events down to a rate which can be recorded for later offline analysis. It reduces the event rate to approximately 200 Hz, with an average event processing time of about 4 s. Once an event is selected by the event filter, it is moved to permanent storage at the CERN computing centre. The average event size is then $\sim$ 1.3 MB.

2.2.7 Trigger tests

The trigger performance have been extensively tested with simulated raw data and cosmic data, but only the availability of high-energy collisions will give a sufficient test of the trigger capabilities. The tests performed on simulated data are done for a variety of

physics processes. Studies have also been made for data simulated with a misaligned and mis-calibrated detector to verify the robustness of the selection. Figure 2.7 is an example of a study made on simulated raw data that first have been passed through the trigger and DAQ systems.

Chapter 3

Data Production and Analysis Tools

The LHC is scheduled to produce its first collisions October 2008. To prepare for this, scientists have been studying simulated data. The advantage of working with simulated data is that it gives you the opportunity to check if your analysis programs actually do what you want them to do. It provides you with some important experiences for when the real data is to be studied (eg. the data contains Monte Carlo truth information that allows for a detailed understanding of the reconstruction software), and it is often useful to compare the real data output with output from the simulated data.

In this chapter I will briefly introduce the main steps of a Monte Carlo generator, and thereafter describe how a detector event is simulated. I will mention the different types of data sets used within the ATLAS collaboration, and also say a few words about Athena, the control framework used by the collaboration. Finally I will give a short introduction to ROOT, the analysis framework used for this thesis.

3.1 Monte Carlo Generators

Event generators are used to reproduce the collision processes taking place in real detectors. They produce hypothetical events based on the distributions predicted by theory [40]. In order to produce a satisfactory result, one needs ever more sophisticated and complex generator codes. For p-p collisions, general purpose showering and hadronisation generators (SHGs), such as PYTHIA [41] and HERWIG [42], are used. The methods employed by the different SHGs may at times differ drastically, but the basic principles are normally the same. Most start off with a leading order ($2 \rightarrow 2$) *hard subprocess*, which is a very simple description of an elementary process. Higher order effects are added by "evolving" the event using the *parton shower*, which allows partons to split into pairs of other partons [40]. The resultant partons are then grouped together, or *hadronized*, into colour-singlet hadrons, and resonances are decayed. Finally the underlying structure of the event is generated. This includes the generation of beam remnants, interactions from other partons in the hadrons, and collisions between other hadrons in the colliding beams (called *pile-up*) [40]. An overview of the different steps taking place, is

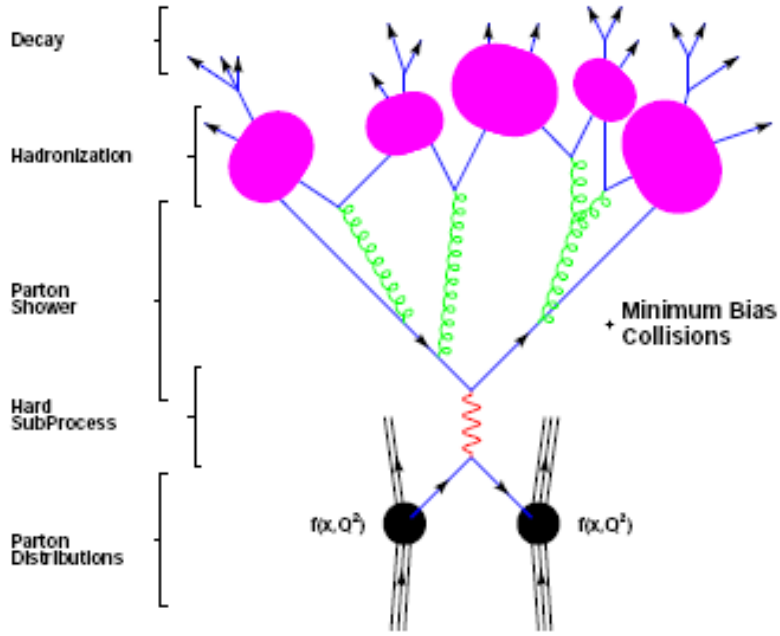

Figure 3.1: Schematic representation of the general structure of a showering and hadronization generator event. For simplicity, showering of the initial state partons is not included in the figure, though it is included in the SHG's. The time evolution of the event goes from bottom to top [40].

shown schematically in Figure 3.1. All centrally produced ATLAS data are generated with PYTHIA.

3.2 Detector Simulation

After an event is generated, the detector effects need to be simulated in one of two ways: Through fast or full simulation. The fast simulation is done using Atlfast [43]. It is (as the name suggests) less time consuming than the full simulation, but it may also produce less accurate results. All the data analyzed in this thesis however, has been produced with full simulation.

The full simulation of ATLAS is done using Geant4. It is a toolkit for simulating the passage of particles through matter, developed in a worldwide collaboration between physicists and software engineers. The toolkit makes use of an object-oriented design, and is written in the C++ programming language[1]. It provides simulation for a large

[1] The source code and documentation is available from the Geant4 Web site [44].

variety of physics processes based on theory, data or parameterisation [45]. In addition it is able to cover a wide energy range, and efficiently handle complex geometries, which is essential in order to simulate the ATLAS experiment.

To best mimic the detector response, the simulation produces hits which can be directly processed by a digitization algorithm and transformed into Raw Data Objects (RDOs). (These should resemble the real detector data.) Alternatively the hits can first be sent to a pile-up algorithm before being passed on to the digitization stage [39]. A schematic representation of the full production chain is shown in Figure 3.2.

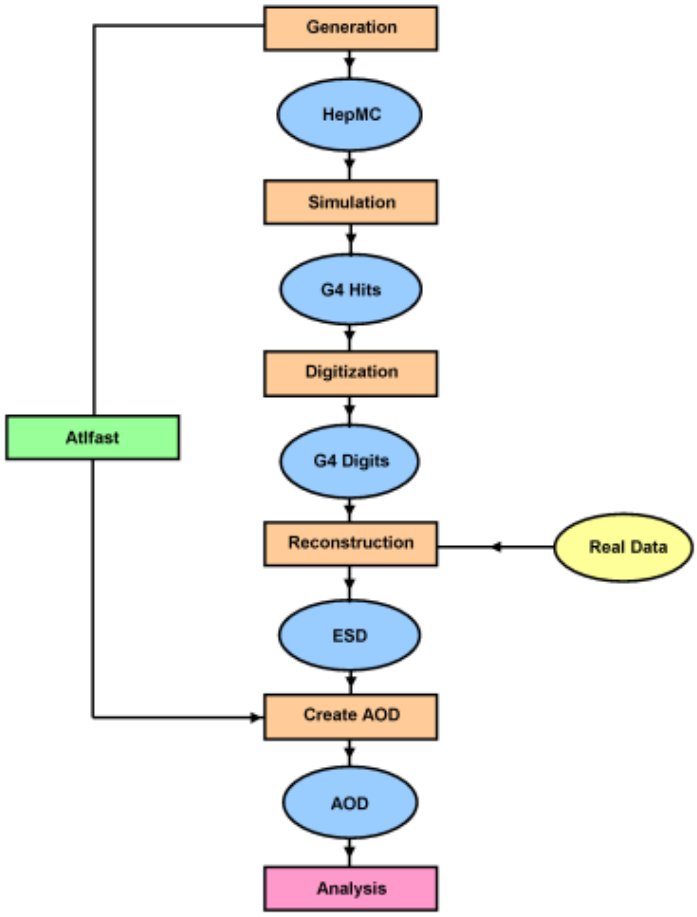

Figure 3.2: The Full Chain Monte Carlo production is shown schematically. The ellipses correspond to the output data, and the rectangles to the different processes that take place. Also indicated are what steps that can be replaced by the fast simulation, and what steps that coincide with the production chain of the real data. The fast simulation can produce the AOD from generated events, simulated events, digitized events or the ESD, since each of these data formats contains the full record of the event generation. The figure is taken from [46].

3.3 Different Data Sets

The large amount of raw data the ATLAS detector will produce each year is not easily distributed to the ATLAS physicists worldwide. To simplify this distribution, several different types of data sets, corresponding to different sizes and levels of information, are produced. The following data sets are available:

- *The Byte-stream Data* is a persistent presentation of the event data flowing from the high-level trigger [39].

- *The Raw Data Object (RDO)* is a C++ object representation of the byte-stream information [39]. The RDO is a digitized representation of the simulated hits that closely resembles the real data.

- *The Event Summary Data (ESD)* is produced from the RDO by processing the latter with a reconstruction algorithm. The role of the reconstruction is

  > ...to derive from the stored raw data the relatively few particle parameters and auxiliary information necessary for physics analysis: photons, electrons, muons, tau-leptons, K^0s, jets, missing transverse energy, primary vertex [39].

  Information from all sub-detectors is combined to optimize the four-momentum reconstruction.

  The target size for the ESD is 500 kB/event, of which most is shared between the Calorimeter Cells and the Tracking [47].

- *The Analysis Object Data (AOD)* is a slimmed down version of the ESD that contains enough information for common analyses. It is usually produced from the ESD, though it is also possible (but ill-advised) to produce it directly from the RDO. The target size for the AOD is 100kB/event, with dominant contributions arising from trigger data objects.

- *The Derived Physics Data (DPD)* is separated into primary DPD (D^1PD), secondary DPD (D^2PD), and tertiary DPD (D^3PD). The D^1PD is obtained directly from the AOD and can be seen as a distilled version of said AOD [47]. It is also possible to regard the AOD as a primary DPD.

  The secondary DPD is derived from the primary DPD. It uses the same format, but contains mostly analysis spesific information.

  The tertiary DPD can be produced either from D^1PD or D^2PD. It is used to produce the final plots of the analysis, and could be in another format. The ROOT Ntuples used for the analysis in this thesis is an example of a tertiary DPD.

3.4 The Athena Framework

The Athena framework is an enhanced version of the Gaudi framework [48], which was originally developed by the LHCb experiment. Nowadays the Gaudi project is a software kernel common to both LHCb and ATLAS, and it is being co-developed by the two experiments. Athena is the sum of this kernel and some ATLAS specific enhancements [49].

All levels of processing of ATLAS data, from high-level trigger to event simulation, reconstruction and (to some extent) analysis, take place within the Athena framework [39]. This ensures that all types of applications (simulation, reconstruction etc.) use the same geometry and conditions data. The framework is designed upon a principle of clear separation between algorithms and data objects. Data objects are "small" objects that contain essentially mathematical quantities like hits, vectors, points etc., while algorithm objects are more complex entities used to manipulate the data objects [50].

3.5 The ROOT Framework

ROOT is an object-oriented framework aimed at solving the data analysis challenges of high-energy physics (HEP) [51]. In addition to basic utilities and services, such as Input/Output (I/O) and graphics, ROOT also provides a large selection of analysis specific utilities such as histograms and fitting. It consists of two main parts: The ROOT libraries and CINT. CINT is a C++ interpreter, and is an independent product ROOT uses for comand line and script processors. This means that with CINT one can run small C++ scripts without compiling the code.

The ROOT libraries are developed to make physics analysis easier for the user. They are organized in a way that minizes dependecies, meaning that one can load just enough code for the task at hand rather than having to load all libraries or one monolithic chunk [51]. The pre-made classes include everything from graphics displays to vector calculations, and help make the analysis more about physics and less about programming.

Chapter 4

$B_s^0 \rightarrow J/\psi\,\phi \rightarrow \mu^+\mu^- K^+ K^-$

In this chapter we will try to reconstruct the B_s mass in $B_s \rightarrow J/\psi\phi \rightarrow \mu^+\mu^- K^+ K^-$, using data from the official ATLAS production. We will first examine the signal separately, before later introducing two relevant types of background processes: Generic B decays, $bb \rightarrow \mu^+\mu^- X$, where the two muons in most cases come from a J/ψ, and events where a J/ψ is produced directly from the p-p collision, $pp \rightarrow J/\psi(\mu^+\mu^-)X$. Selection criteria for different observables will then be investigated, and the B_s mass reconstructed from the combined samples.

The study is performed using root ntuples developed from AODs.

4.1 Invariant Mass Reconstruction

From Einsteins theory of special relativity we know that a particle's energy can be expressed in terms of its mass and its momentum [1]:

$$E^2 = p^2c^2 + m^2c^4 \,, \tag{4.1}$$

where E is the energy of the particle, p its momentum, m its mass, and c is the speed of light ($\approx 3 \cdot 10^8$ m/s). In particle physics one usually uses natural units, in which $c = 1$ and can be omitted from the above expression.

Assuming a particle is stable, we can determine its mass directly from Equation 4.1 by measuring its energy and momentum. However, most of the particles we detect are highly unstable and can only be observed through their decay products. To determine the masses of these particles, we introduce a quantity called invariant mass. For n final state particles it is given by [1]

$$M^2c^4 \equiv \left(\sum_{i=1}^{n} E_i\right)^2 - \left(\sum_{i=1}^{n} \boldsymbol{p}_i\right)^2 c^2 \,, \tag{4.2}$$

where M is the invariant mass and E_i ($\boldsymbol{p}_i$) is the energy (momentum) of particle i. Energy-momentum conservation dictates that the mass of the decaying particle is equal

to the invariant mass of its decay products, meaning that we can use the latter to determine the former if a particle is too short-lived for its mass to be measured directly. In the following analysis we shall exploit this fact to determine the mass of the B_s, using simulated $B_s \rightarrow J/\psi\ \phi$ events in ATLAS. For simplicity, we start by examining the signal without any background present.

4.1.1 Reconstructing the B_s Mass from the Signal

The signal sample consists of 14,750 $B_s^0 \rightarrow J/\psi\phi$ events, where the J/ψ is forced to decay to two oppositely charged muons and the ϕ to two oppositely charged kaons.

The J/ψ Mass Spectrum

When trying to reconstruct the mass of the B_s, we start by searching for two oppositely charged muons with minimum p_T values of 6 and 4 GeV, originating from a common vertex in the detector. In the signal sample there are usually between two and three muons per event. This means that we get a very narrow peak when reconstructing the di-muon invariant mass, even if we allow for all combinations of muons and employ no additional requirements than the ones already mentioned, as can be seen from Figure 4.1a. In Figure 4.1b we have in addition tightened the quality criteria on the muon tracks. Both the matching of the ID tracks with the muon spectrometer tracks, and the fit of the tracks to the data points are required to have a $\chi^2/dof \leq 4.0$. These hardly have any impact on the signal efficiency. They remove background from misidentified muons, which will be important when we start looking at real collisions. In the latter figure, we have selected only one J/ψ candidate per event (the one that together with the ϕ gives the best B_s vertex quality).

To determine the mass of the J/ψ, the muon distribution has been fit to a Gaussian function [51]

$$f(x) = p_0 \cdot \exp\left(-\frac{1}{2}\cdot\left(\frac{x-p_1}{p_2}\right)^2\right)\ ,\ x \in [2800, 3400]\ , \tag{4.3}$$

where p_0 is a constant term, p_1 is the mean, μ, and p_2 is the standard deviation, σ. The fit gives a mean value of (3101.7 $\pm$ 0.9) MeV with a (65.34 $\pm$ 0.64) MeV standard deviation. Compared to the PDG value of (3096.916 $\pm$ 0.011) MeV [17], this is slightly high, but well within one sigma deviation.

The ϕ Mass Spectrum

After a J/ψ candidate has been selected, we start looking for tracks in the nearby calorimeter regions. In ATLAS there is no identification of hadronic particles, so all hadronic tracks in the following are assumed to be kaons, even though this is far from the truth. Most of them are actually pions, which are the lightest mesons and hence the easiest to

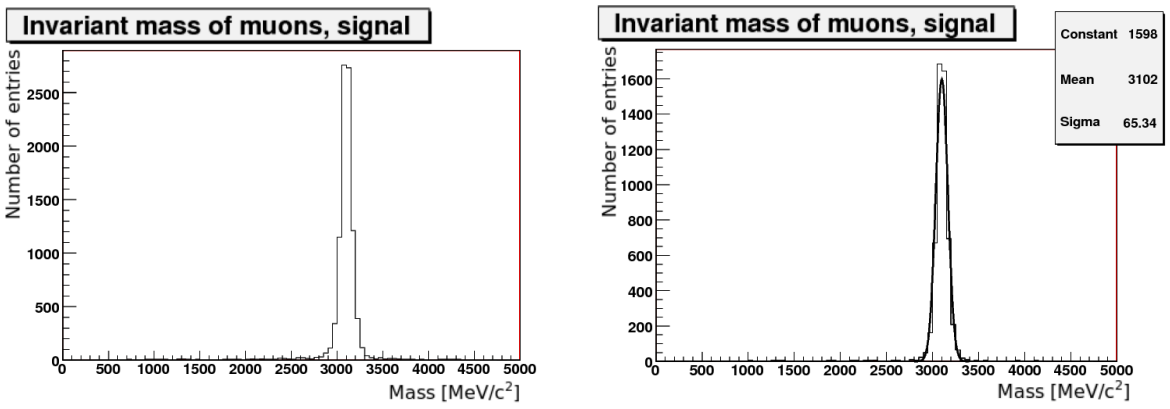

(a) *(b)*

Figure 4.1: The reconstructed J/ψ mass (a) for all combinations of muon pairs, and (b) after picking the "best" B_s candidate in each event and including some simple selection criteria (see text). In (b) a Gaussian fit (Equation 4.3) has been imposed to determine the J/ψ mass.

produce. When the initial b-quark hadronizes, many excess particles are produced in addition to the B_s meson (see Section 3.1 for details on the generation process). Each signal event contains on average around 40 hadron tracks. This, together with the lack of particle identification, makes the ϕ much harder to identify than the J/ψ, even if we evaluate the signal only. Figure 4.2a shows the invariant mass of all combinations of kaon pairs, while Figure 4.2b shows the reconstructed mass of the ϕ candidate that, together with the J/ψ, gives the best vertex quality for the B_s. We notice that the latter requirement drastically reduces the number of wrong combinations, but that the peak is nevertheless fairly wide, as is expected for all decay modes in ATLAS.

The shape of the histogram is fitted using the sum of a Gaussian function (to describe the peak) and a first order polynomial (to explain the underlying structures)

$$f(x) = p_3 + p_4 \cdot x + p_0 \cdot \exp\left(-\frac{1}{2} \cdot \left(\frac{x - p_1}{p_2}\right)^2\right) \ , \ x \in [990, 1070] \ , \tag{4.4}$$

where p_3 gives the intersection between the polynomial fit and the y-axis, p_4 is the slope of the polynomial, and p_0-p_2 are the parameters of the Gaussian fit described in Equation 4.3. The Gaussian peak is required to be between 1010 and 1030 MeV. The combined fit then gives a ϕ mass of (1019.5 ± 0.1) MeV with a (5.104 ± 0.187) MeV standard deviation, which corresponds nicely to the PDG value of (1019.455 ± 0.020) MeV [17].

The B_s Mass Spectrum

To determine the B_s mass, we now combine the selected kaon and muon tracks and calculate their invariant mass, again using Equation 4.2. Figure 4.3b shows the mass spectrum after an additional requirement on the J/ψ mass ($\pm$ 3σ) and one on the ϕ

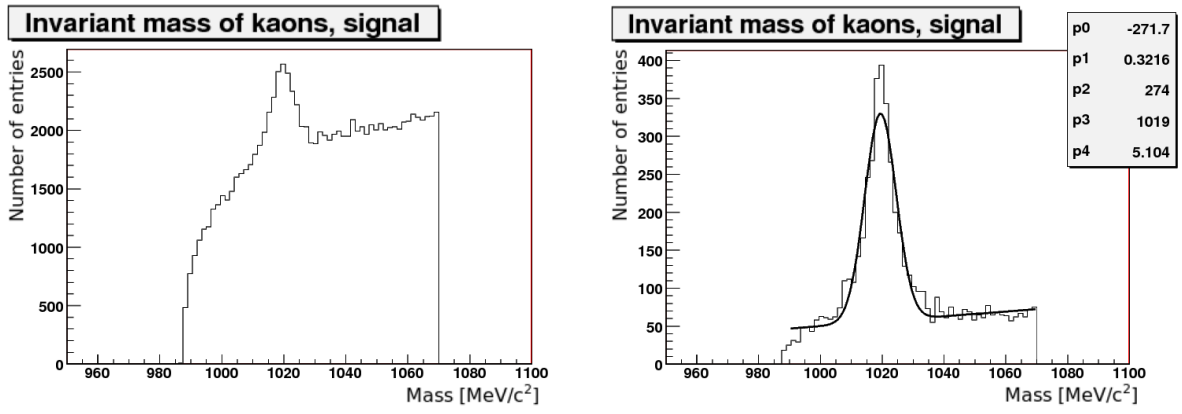

(a) *(b)*

Figure 4.2: The reconstructed ϕ mass (a) for all combinations of kaon pairs, and (b) after picking the "best" B_s candidate in each event and including some simple selection criteria (see text). In (b) a fit to a Gaussian plus a first order polynomial (Equation 4.3) has been imposed to determine the ϕ mass. The names of the fit parameters are interchanged with respect to the discussion in the text. Here p_0-p_1 describes the polynomial and p_2-p_4 describes the Gaussian peak.

mass ($\pm$ 2σ). Here a Gaussian fit (Equation 4.3) has also been imposed, giving a mean mass of (5368.7 $\pm$ 2.1) MeV with a (106.7 $\pm$ 1.5) MeV standard deviation. The mean value is close to the expected mass of (5366.3 $\pm$ 0.6) MeV [17]. For comparison, the reconstructed mass before cuts is shown in 4.3a.

4.2 The Background Samples

For this analysis, two separate types of background processes have been investigated. The first, which we shall henceforth refer to as generic B background, contains 143,750 processes of the kind $bb \rightarrow \mu^+\mu^- X$ and $bb \rightarrow J/\psi(\mu^+\mu^-)X$. Since they contain B mesons, they are very similar to the signal decay, and hence the hardest to get rid of. The second type of background studied, we shall call direct J/ψ background. It contains 40,425 processes in which a J/ψ is produced directly from the pp collision together with some extra particle or particles, $pp \rightarrow J/\psi(\mu^+\mu^-)X$. The J/ψ can here be combined with two of the many hadronic tracks in the detector to form a (wrong) B_s candidate. This background is easily separated from the signal by introducing a requirement on the transverse vertex displacement, L_{xy}, of the so-called B_s. The displacement is defined as the distance in the x-y plane to the primary vertex from the point of closest approach.

Other useful quantities include the already mentioned B_s vertex quality, and the B_s pointing angle. The latter is defined as the direction of the combined $\mu^+\mu^-K^+K^-$ track compared to the direction of the B_s boost. In the following section we will explain how these variables (and others) can be used for background rejection.

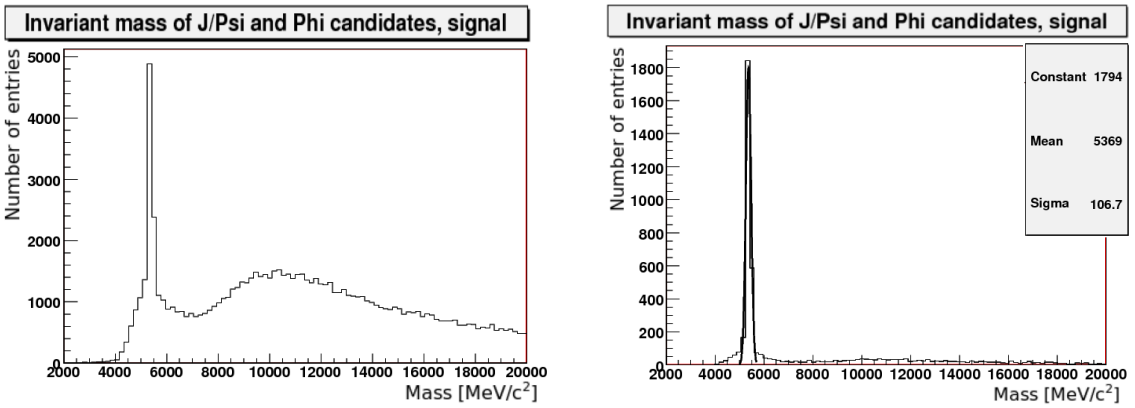

(a) *(b)*

Figure 4.3: The reconstructed B_s^0 mass (a) for all combinations of muon and kaon pairs, and (b) after picking the "best" candidate in each event and including some simple selection criteria (see text). The solid line shows the imposed Gaussian fit.

4.3 Signal Selection

For the signal selection we investigate four observables: The pointing angle of the B_s meson, its transverse vertex displacement, its vertex quality, and the transverse momentum of the kaon tracks. Figure 4.4a shows normalized histograms of the transverse vertex displacement for signal and backgrounds. The signal is shown in black, and the backgrounds in red (generic B background) and blue (direct J/ψ background). Figure 4.4b shows a 2D scatter plot of the $\mu^+\mu^-K^+K^-$ invariant mass versus the transverse vertex displacement (signal in black, combined background in red). From 4.4a we learn that the vertical band in 4.4b mostly contains direct J/ψ events. Requiring $\mathrm{L_{xy}} > 0.4$ removes most of the background without loosing much signal.

Figure 4.5 shows the same two plots for the transverse momentum of the lowest p_T kaon candidate. The signal is in black and the background in red. In both plots we see a cut-off at 0.5 GeV. This is due to a requirement made in the reconstruction. Figure 4.5b suggests that a large fraction of the low p_T tracks from the signal events are wrongfully chosen, which explains part of the similarity between the signal and background structure in (a). A p_T requirement around 1.0 GeV seems prudent, but we would, of course, have to check for correlations before employing both the p_T and the $\mathrm{L_{xy}}$ requirement at the same time. This will be done in the next section. Here, we investigate the four observables independently of each other.

Figure 4.6 shows the B_s vertex quality for signal and background, and the $\mu^+\mu^-K^+K^-$ invariant mass versus the vertex quality. The entries of negative vertex quality are probably due to an error in the simulation/reconstruction, and will be disregarded when we later reconstruct the $\mu^+\mu^-K^+K^-$ invariant mass. Because the background in these plots is dominated by the generic B decays, it is expected that the vertex quality distributions

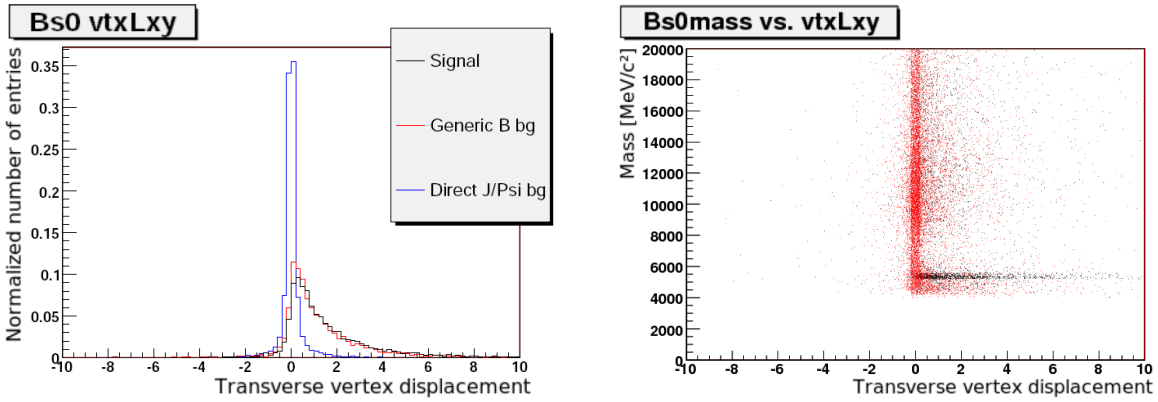

(a) *(b)*

Figure 4.4: (a) Normalized histograms of the B_s transverse vertex displacement, and (b) scatter plot of the B_s mass vs. the same variable. The signal is shown in black, and the background in red/blue. In (b) no distinction is made between the direct J/ψ background and the generic B background and they are both shown in red.

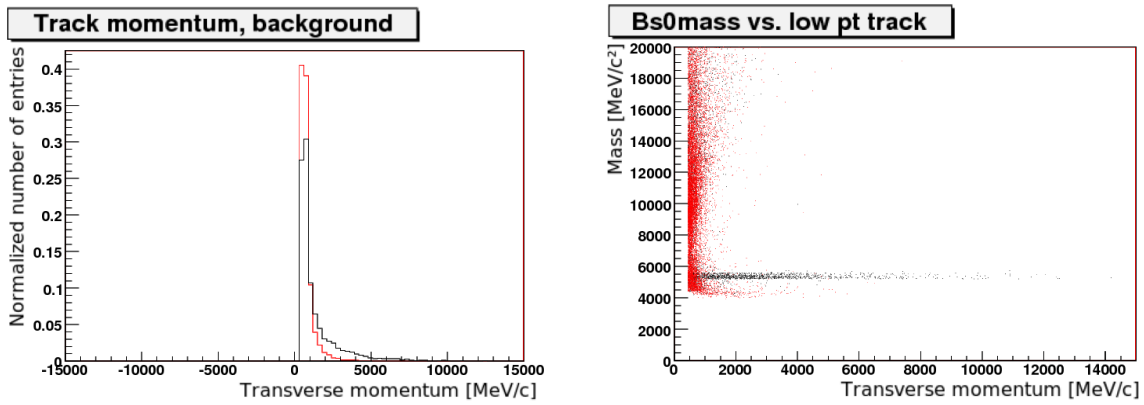

(a) *(b)*

Figure 4.5: (a) Normalized histograms of the p_T of the lowest p_T kaon tracks, and (b) scatter plot of the B_s mass vs. the same variable. The signal is shown in black, and the background in red.

look similar for signal and background. It is however, important to require a good vertex to reduce the amount of wrongly combined tracks. Especially if one considers real data, where there will be a large number of additional tracks present from pile-up and underlying events. Figure 4.7 investigates the possible effect of a pointing requirement. The entries with negative pointing angle is a resolution effect due to the fact that we combine random candidates. Requiring a pointing angle below 0.5 removes much of the background, while keeping most of the signal.

Other observables have, of course, also been investigated, but the ones above were the ones that in the end were optimized and used. Observables that might be useful, but have not yet been investigated, are the isolation and the flight length significance (defined as $\frac{d}{\sigma_d}$, where d is the distance the particle travels).

4.4 Correlations

To check if there are correlations between the observables discussed above, we here look at scatter plots of the four observables versus each other. We also introduce scatter plots of low p_T versus high p_T kaon tracks, since only the low p_T kaons were considered previously. Requirements on transverse momentum are implicit mass requirements, which means we have to be especially careful here.

Figures 4.8, 4.9 and 4.10 shows the pointing angle versus the transverse vertex displacement, the low p_T tracks, and the vertex quality, respectively. Figure 4.11 shows the low p_T tracks versus the vertex quality, and Figures 4.12 and 4.13 shows the transverse vertex displacement versus the low p_T tracks and vertex quality, respectively. The black dots are the signal and the red dots are the background. From the figures it is clear that some slight correlations between the observables exists. From Figures 4.11 - 4.13 it is clear that requirements on L_{xy} and on the p_T of kaon tracks both reduce the effect of an additional vertex quality requirement drastically. In addition we see that they overlap slightly with each other. Requiring a good pointing angle also reduces the effect of a vertex quality requirement (see Figure 4.10). Figure 4.8 and 4.9 shows overlaps between possible pointing angle and displacement requirements, and between possible pointing angle requirements and selections based on the transverse momenta of kaon tracks, respectively.

Because a selection based on one observable influences that of the others, we show the $\mu^+\mu^-K^+K^-$ mass versus the various observables once more. This time a selection on the previous observables has been introduced between each plot. Figure 4.14 is the same as Figure 4.7 of Section 4.3. It shows the reconstructed mass versus the B_s pointing angle. Based on this 2D representation, we require a B_s pointing angle below 0.5 before reconstructing Figure 4.15, which shows the mass versus the transverse vertex displacement after this additional requirement. A vertical band of background events dominates at lower values of the displacement, and we require $L_{xy} \geq 0.4$. Figure 4.16 shows the reconstructed mass versus the transverse momenta of the low p_T kaon tracks after this selection was made. We notice that the background is drastically reduced com-

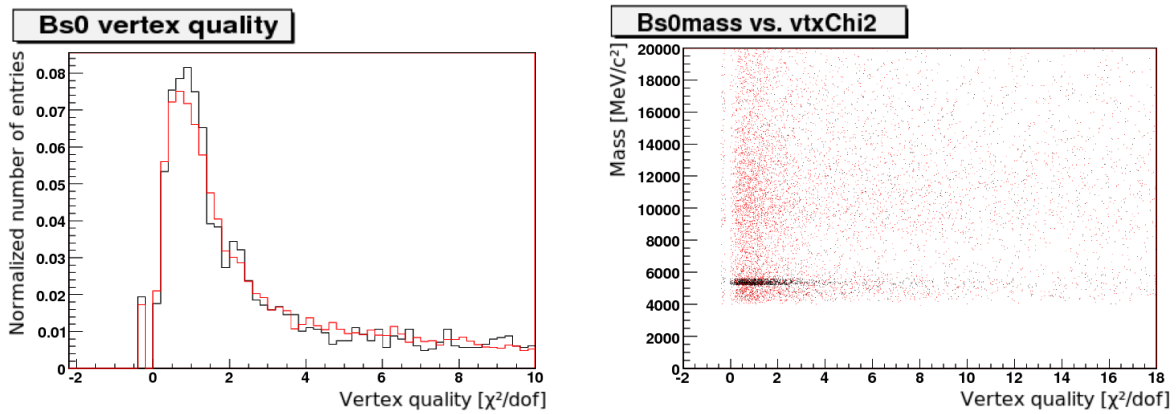

(a) *(b)*

Figure 4.6: (a) Normalized histograms of the B_s vertex quality, and (b) scatter plot of the B_s mass vs. the same variable. The signal is shown in black, and the background in red.

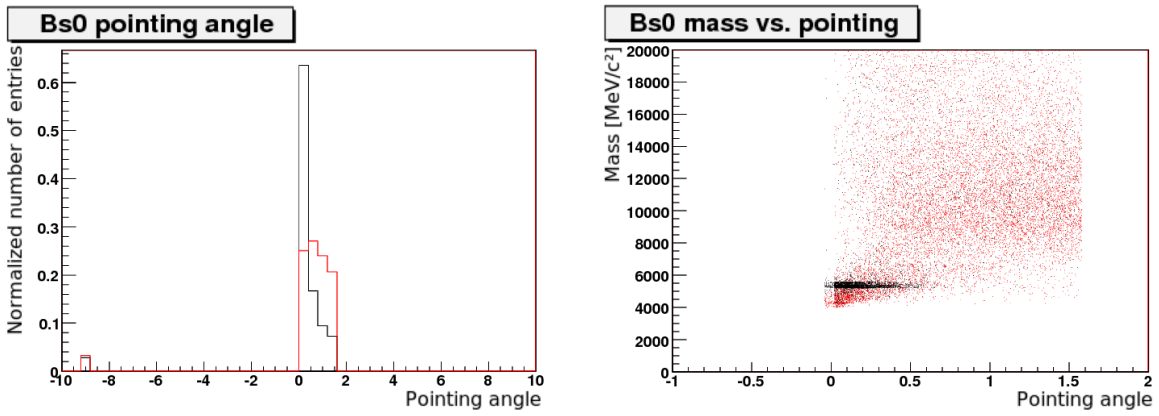

(a) *(b)*

Figure 4.7: (a) Normalized histograms of the B_s pointing angle, and (b) scatter plot of the B_s mass vs. the same variable. The signal is shown in black, and the background in red.

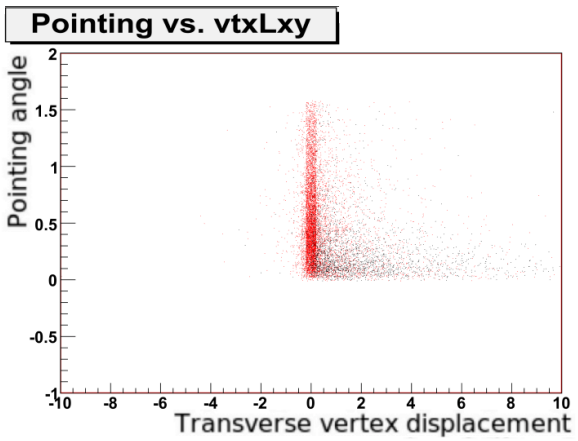

Figure 4.8: Scatter plot of the B_s pointing angle versus the transverse vertex displacement of the B_s.

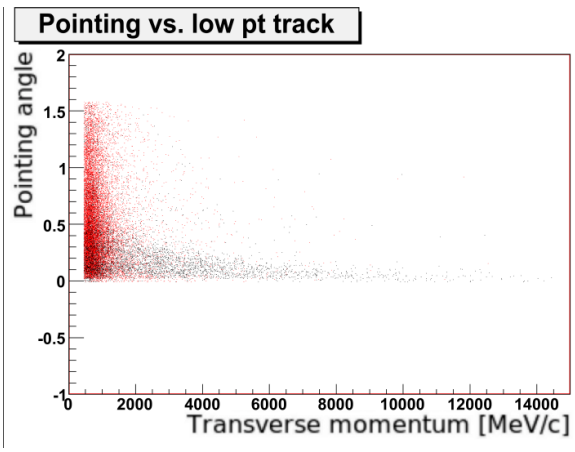

Figure 4.9: Scatter plot of the B_s pointing angle versus the low p_T tracks.

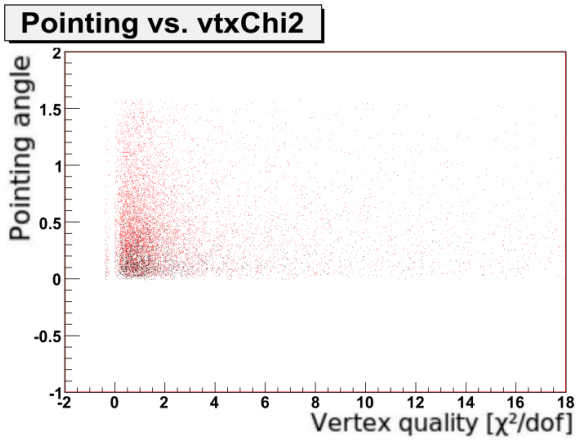

Figure 4.10: Scatter plot of the B_s pointing angle versus B_s vertex quality.

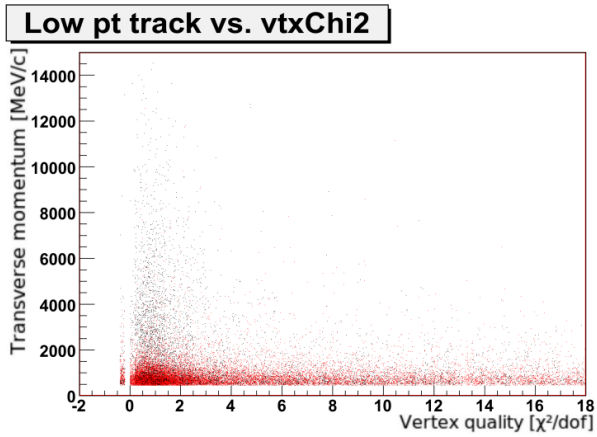

Figure 4.11: Scatter plot of the low p_T tracks versus the B_s vertex quality.

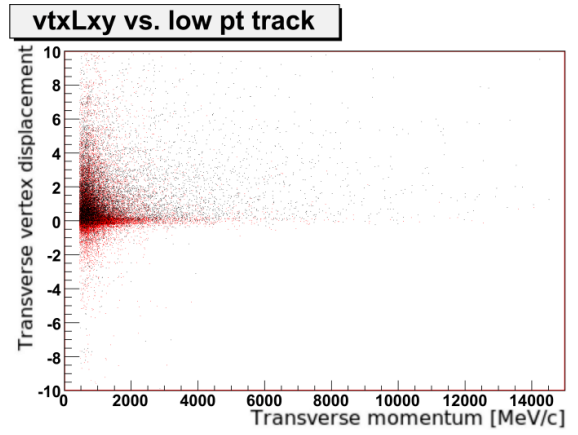

Figure 4.12: Scatter plot of the transverse vertex displacement of the B_s versus the low p_T tracks.

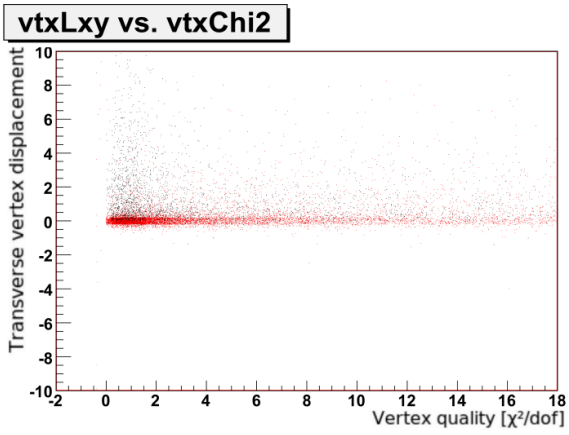

Figure 4.13: Scatter plot of the transverse vertex displacement of the B_s versus the B_s vertex quality.

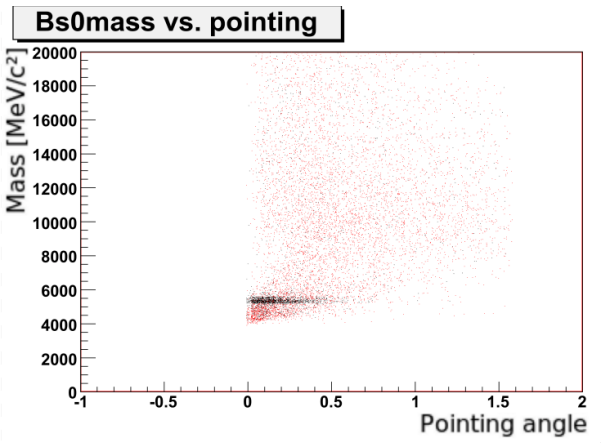

Figure 4.14: Scatter plot of the $\mu^+\mu^-K^+K^-$ invariant mass versus the pointing angle

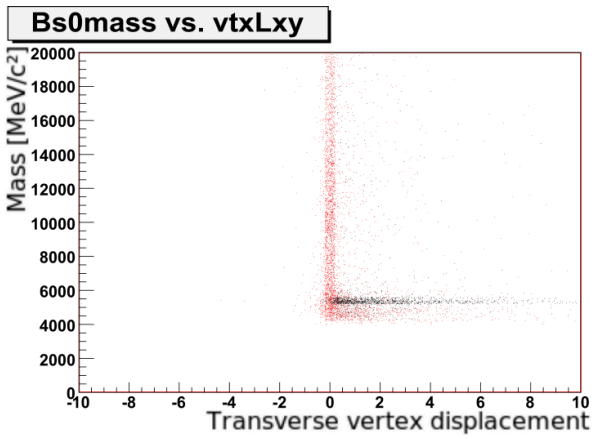

Figure 4.15: Scatter plot of the $\mu^+\mu^-K^+K^-$ invariant mass versus the transverse vertex displacement after requiring pointing ≤ 0.3.

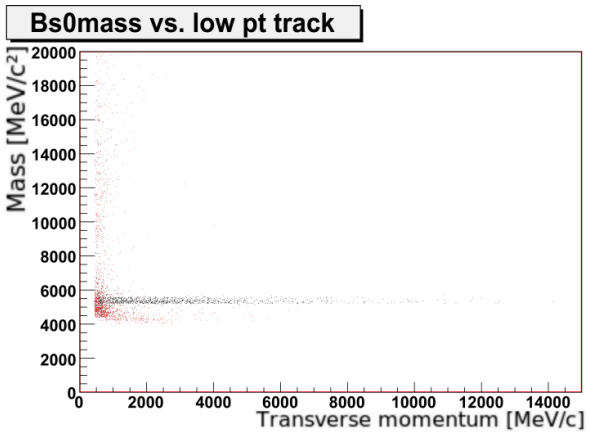

Figure 4.16: Scatter plot of the $\mu^+\mu^-K^+K^-$ invariant mass versus the transverse momenta of the low p_T kaon tracks after requiring pointing ≤ 0.3 and $L_{xy} \geq 0.4$.

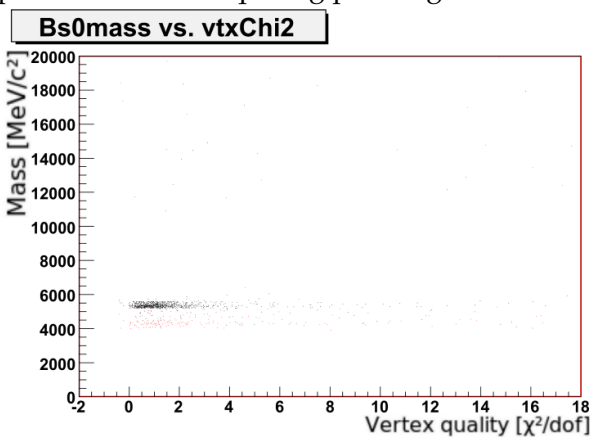

Figure 4.17: Scatter plot of the $\mu^+\mu^-K^+K^-$ invariant mass versus the vertex quality after requiring pointing ≤ 0.3, $L_{xy} \geq 0.4$ and kaon $p_T \geq 0.9$ GeV.

pared to Figure 4.5. Figure 4.11 shows the mass versus the vertex quality of the B_s after also requiring a minimum p_T of 0.9 GeV for all kaon tracks. We see that a vertex quality requirement at this point will have little or no effect on the reconstructed $\mu^+\mu^-K^+K^-$ mass spectrum. In the following we will see that the requirements made thus far closely resembles the optimized requirements that in the end is used when reconstructing the B_s mass (Section 4.5).

Figure 4.18 shows the transverse momenta of the low p_T kaon tracks versus the high p_T kaon tracks for signal (a) and background (b). Only the AOD requirements, given at the beginning of this chapter, are enforced. The momenta are highly correlated. In the signal sample we expect some correlation since the two tracks ideally come from

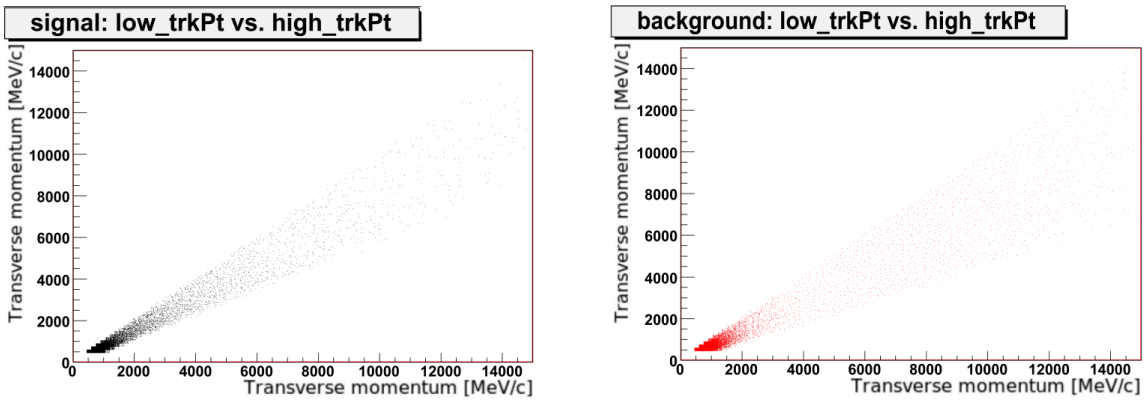

(a) *(b)*

Figure 4.18: Transverse momenta of the low p_T kaon tracks versus the high p_T kaon tracks for signal (a) and background (b).

the same decaying ϕ. However, looking back at Figure 4.2a, we remember that also the signal sample contains a large number of hadronic tracks that do not come from a decaying ϕ. This means that though one expects the track momenta to be correlated, the correlation seen in Figure 4.18a seems slightly high. Figure 4.18b shows a strong correlation is present also in the background samples, which is very unexpected. The reason for these strong correlations is a mass requirement made on AOD level. When combining two tracks to form a ϕ candidate, the invariant mass is required to be between 970 MeV and 1070 MeV. Loosening this mass requirement, decreases the correlations, while tightening it increases the correlations.

4.5 Reconstructing the B_s mass from signal + background

When combining the signal and background samples, we need to introduce a weighting scheme in order to ensure that the signal-background ratio is the same as what is expected in ATLAS. In this analysis, the signal is left as it is, and the respective backgrounds are weighted to match it. The weights are given by

$$w = a \cdot \frac{\int \text{initial signal histogram}}{\int \text{initial background histogram}} \,. \tag{4.5}$$

where w is the weight that the background events are multiplied by, and a is a normalization factor based on the cross-sections of the respective processes.

Figure 4.19 shows the reconstructed $\mu^+\mu^-K^+K^-$ invariant mass for the combined signal and weighted backgrounds, for all combinations of tracks. For comparison, the signal histogram is shown separately in black. It is apparent that good selection criteria is needed for the B_s mass peek to become visible.

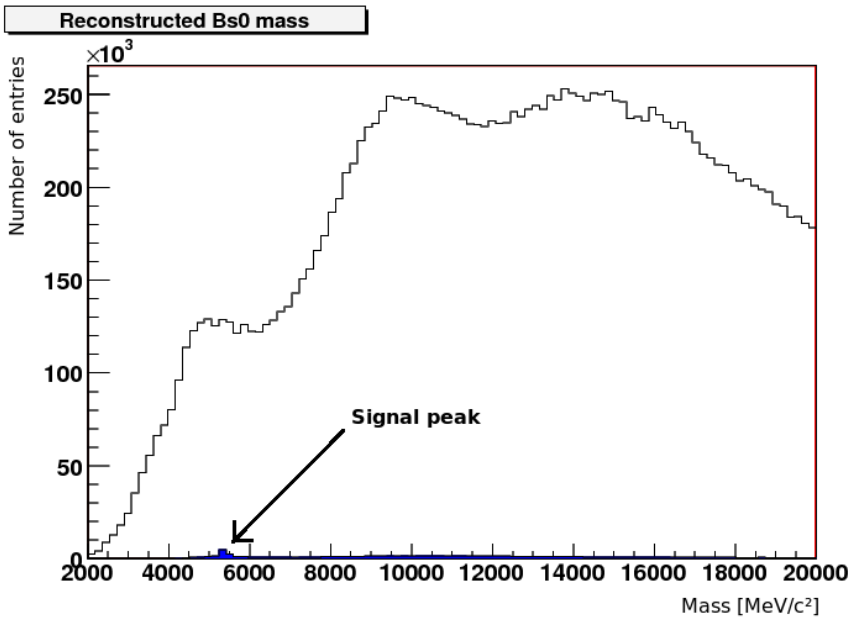

Figure 4.19: The reconstructed B_s mass from the combined signal and background samples before any criteria are introduced. To illustrate the size of the signal, its histogram is shown separately in black.

4.5.1 Sensitivity

Though the B_s mass, in principle, could be reconstructed using the requirements discussed in Section 4.4, we would like to optimize the selection criteria before doing the reconstruction. We therefore introduce a parameter called the sensitivity, given as the ratio

$$R = \frac{\#\text{signal events}}{\sqrt{\#\text{signal events} + \#\text{background events}}}\,. \tag{4.6}$$

The idea is to remove as much background as possible while keeping most the signal. Figure 4.20 shows the sensitivity for various pointing requirements at an integrated luminosity of 1 fb^{-1}, after employing the criteria listed in Table 4.1. Only the mass window between 5100 MeV and 5700 MeV is considered. The selection is placed where the graph stops to rise, at 0.3.

Figure 4.21 shows the sensitivity as a function of the transverse vertex displacement of the B_s after the criteria in Table 4.1 and a requirement on the B_s pointing angle of 0.3 are employed. Based on the figure, we require $L_{xy} \geq 0.4$. Figure 4.22 shows the sensitivity for various values of the kaon p_T after all the requirements discussed. A requirement of $p_T \geq 0.9$ GeV is selected. An additional requirement for the B_s vertex

Observable	Criteria
Muon transverse momentum	$\geq 4 + 6$ GeV
Fit of muon tracks, χ^2/dof	< 4.0
J/ψ mass	$\mu \pm 3\sigma$ (from fit)
Best pointing angle of B_s	—

Table 4.1: List of the criteria used when investigating the sensitivity of the discussed observables.

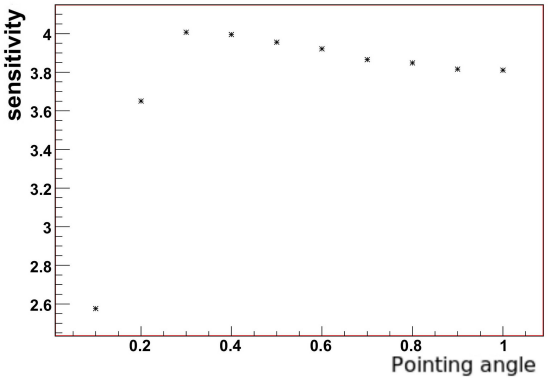

Figure 4.20: Sensitivity as a function of the B_s pointing angle.

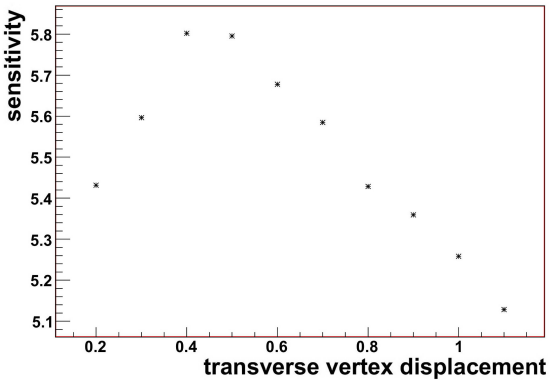

Figure 4.21: Sensitivity as a function of the transverse vertex displacement of the B_s after a pointing requirement is made.

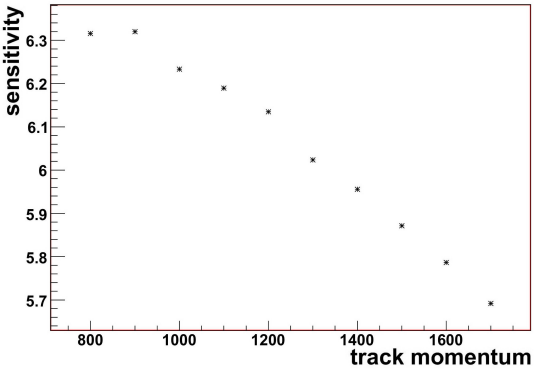

Figure 4.22: Sensitivity as a function of low p_T kaon tracks after requiring a pointing ≤ 0.3 and a displacement ≥ 0.4.

quality at this point, will not improve the sensitivity, and has been left out.

Table 4.2 lists the optimized selection criteria and the sensitivity after each new criteria is introduced.

Observable	Optimized Criteria	Sensitivity
Pointing angle of B_s	≤ 0.3	4.01
Transverse vertex displacement	≥ 0.4	5.80
Kaon transverse momentum	≥ 0.9 GeV	6.32

Table 4.2: List of the optimized selection criteria, and the sensitivity after each new criteria is introduced.

4.5.2 The B_s mass

Based on the criteria listed in Tables 4.1 and 4.2 we now reconstruct the B_s mass (Figure 4.23). A $\pm 2\sigma$ requirement on the ϕ mass has also been implemented. The large spikes at the left of the mass peak are single events from the generic B background. The spikiness result from the scaling of the background for individual events. It is clear that when this few events are present, the weighting introduced leads to some odd features. To avoid this, one could reconstruct the mass with looser selection requirements, and model the shape of the background from that plot. Then one could distribute the approximately 100 events that the background in Figure 4.23 corresponds to, according to that model. However, since the background events are located at the side of the peak, it is not necessary to do so at this point. The histogram is fitted using the sum of a zeroth order polynomial and a Gaussian function (described by Equation 4.4 if one leaves out the second term). From the fit we obtain a B_s mass of (5376.2 $\pm$ 2.6) MeV with a (58.6 $\pm$ 2.4) Mev standard deviation, which is slightly higher than the PDG value of (5366.3 $\pm$ 0.6) MeV [17]. This seems to be due to an over-correction in the calorimeter or muon spectrometer reconstruction algorithms. We remember from earlier that also the reconstructed J/ψ mass was slightly high, while the ϕ mass was closer to the expected value. Reconstructing the mass using only the ID information gives a mass around the PDG value, which verifies that the problem is with the calorimeter or muon spectrometer.

4.6 Final Remarks

We have in this chapter reconstructed the B_s mass for simulated $B_s \rightarrow \mu^+\mu^-K^+K^-$ events in ATLAS. Two separate types of background have been introduced, and we have seen that we can efficiently reduce these backgrounds by employing some very simple selection criteria. The obvious next step would be to model the background in Figure 4.23 as described above. In addition we would like to perform a sideband study of the separate backgrounds.

When this is done, one might also consider doing a multivariate analysis, e.g. a boosted decision tree or a neural net, and see if this can improve the results further.

In time, (when the detector is well understood and a sufficient amount of data has

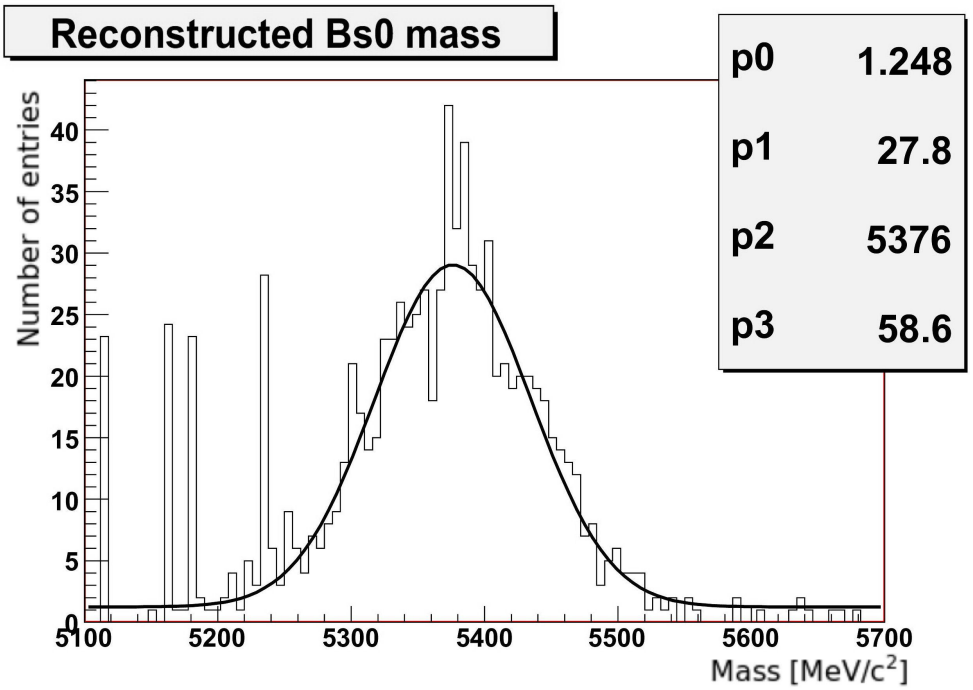

Figure 4.23: The reconstructed $\mu^+\mu^-K^+K^-$ invariant mass after optimizing the selection criteria. The solid line shows the fit to a zeroth order polynomial plus Gaussian function. The names of the fit parameters are interchanged with respect to the discussion in the text. Here p_0 is the zeroth order polynomial and p_1-p_3 describes the Gaussian peak.

been collected) the goal is to perform an angular analysis and study the lifetime difference of the two CP eigenstates, B_s^H and B_s^L, as mentioned in Section 1.5.

Chapter 5

Physics Validation

Physics validation is an important tool both for simulated and real data. By studying well known structures, in the case of this analysis the J/ψ mass in $J/\psi \rightarrow \mu^+\mu^-$, we acquire valuable insight into the detector performance. In high-energy proton-proton collisions (like the ones we will have in ATLAS) there is always a huge amount of background present. Because of this complication, it is especially important to study known processes and get a thorough understanding of all possible detector effects before attempting to look for new physics. In this section I will describe a simple method to investigate variations of the J/ψ mass in the different detector regions, using a data sample of 89,000 J/ψ events (49,000 J/ψ from $bb \rightarrow J/\psi(\mu^+\mu^-)X$ and 40,000 from $pp \rightarrow J/\psi(\mu^+\mu^- X)$.

5.1 Reconstruction Efficiency

Since this study is performed on simulated data, we start off by examining the muon reconstruction efficiency. The reconstruction efficiency is, as the name suggests, a measure of how well the reconstruction (and simulation) algorithms do, compared to the Monte Carlo information they start off with. Mathematically, it is defined by

$$\epsilon = \frac{\#\text{ reconstructed muons}}{\#\text{ generated muons}} \,. \tag{5.1}$$

Because of an issue with the reconstruction (it reconstructed some muons twice), the reconstruction efficiency was originally larger than one for some values of η. Therefore, the distance, ΔR, between all combinations of muon tracks, was investigated. If a pair of same charge muon tracks were closer than $\Delta R = 0.2$, the lowest-p_T muon was disregarded in the rest of the analysis. In addition, a very loose quality requirement of $\chi^2/dof \leq 8.0$, was introduced for the fit of the reconstructed tracks. Figure 5.1 shows the muon reconstruction efficiency as a function of pseudorapidity for four different momentum regions after these requirements were employed. The dips around $\eta = 0$ and $|\eta| = 1.4$ correspond to transition regions in the detector. The inefficiency at zero

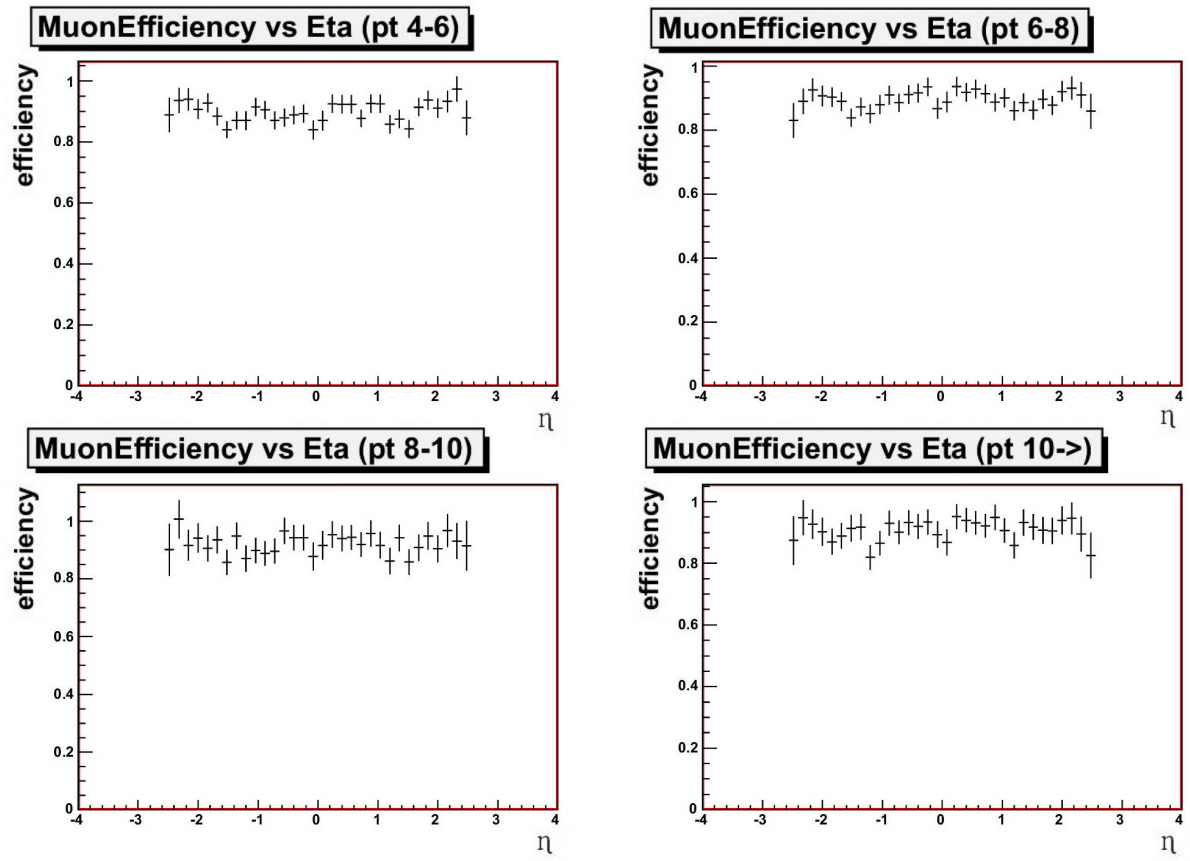

Figure 5.1: The reconstruction efficiency as a function of pseudorapidity for muons in the p_T-regions [4,6) GeV (upper right), [6,8) GeV (upper left), [8,10) GeV (lower right) and [10,→) GeV (lower left). The reconstruction efficiency is defined in Equation 5.1. The dips around $|\eta| = 0$ and 1.4 correspond to transition regions in the detector (see text). Only the detector region of $|\eta| < 2.5$ was considered.

is caused by the feet of the ATLAS detector and by services, like cables and cryogenic lines, to the inner detector components, while the drop around $|\eta| = 1.4$ is caused by the extra material introduced at the transition region between the barrel and end-cap components of the calorimeters. Due to the limitations of the ATLAS detector at large values of $|\eta|$, only the region $|\eta| < 2.5$ is considered. The final dips (at $|\eta| \approx 2.5$) are due to these detector limitations in the area close to the beam pipe.

Based on the dips and rises in the efficiency plots (Figure 5.1), the detector is divided into five positive and five negative η-regions:

$$|\eta| \in [0, 0.2), [0.2, 1.3), [1.3, 1.5), [1.5, 2.0), \text{ and } [2.0, \rightarrow) \ , \tag{5.2}$$

where a square bracket indicates that the corresponding value is included in the interval. The values associated with a parenthesis is not. The arrow in the last interval indicates that the it contains all possible values above the given starting value.

The separation between positive and negative values of η is technically not necessary since the detector is supposed to be symmetric about $\eta = 0$. However, it is always a good idea to test the data against what we think we know to be true. The observant reader might also notice that the regions defined are not of equal size. The reason for choosing not to divide the regions between the dips any further, is simply a desire to improve the statistics wherever possible, and the results should in principle not be affected by this choice.

5.2 Mass Reconstruction

The J/ψ mass was constructed, with the requirement that the two muons be of opposite charge and located within the same η-region. In addition, at least one of the muons was required to be in the desired p_T-region[1], defined as

$$p_T \in [4,6), [6,8), [8,10), \text{ and } [10,\rightarrow) \; . \tag{5.3}$$

Figure 5.2 shows an example of the J/ψ mass plots, made for the five negative η-regions in combination with the four different p_T-regions. In order to determine the mass of the J/ψ, the distributions were fitted to a Gaussian function (Equation 4.3) over the interval [3.0 GeV,3.2 GeV]. In some regions the statistics are a bit low, but in general both the mean and the width of the distribution looks good. Because of the lacking statistics, only one of the muons are required to be in a given p_T region. With the naked eye, we also observe that the width of the peak broadens as $|\eta|$ increases (as expected from Chapter 2). To investigate possible additional effects, the fit parameters are extracted and presented graphically in Figures 5.3 and 5.4. For simplicity, the relevant values are also listed in Table 5.1.

Figure 5.3 shows the fit-parameters as a function of $|\eta|$-region for the different p_T-scenarios, while Figure 5.4 shows the same values as a function of p_T-region for the different intervals of $|\eta|$. Again we notice that the standard deviation becomes larger as $|\eta|$ increases. We also notice that the mass seems to increase slightly with increasing values of $|\eta|$. This is an effect of an over-correction in the reconstruction algorithms. From 5.4 it is clear that no visible dependence upon p_T exists. However, one should keep in mind that only one of the muons were required to be within the selected p_T-regions, and that this would dampen any perceivable effect if one existed. Also in this figure we notice the rise in the J/ψ mass as η increases. Finally, there seems to be a discrepancy between the positive and the negative η-values in regions 3 and 5, where the reconstructed J/ψ mass seems to be higher in the negative pseudorapidity region of the detector. The effect is not very large, and one should also keep in mind that these are the regions where the fit associates the largest errors. However, if these were real data, an effect like this would need to be thoroughly investigated, though in this case it is most likely an effect of the low statistics in these regions.

[1] Unfortunately there were not enough J/ψ events available to require both muons to be in the same p_T-interval.

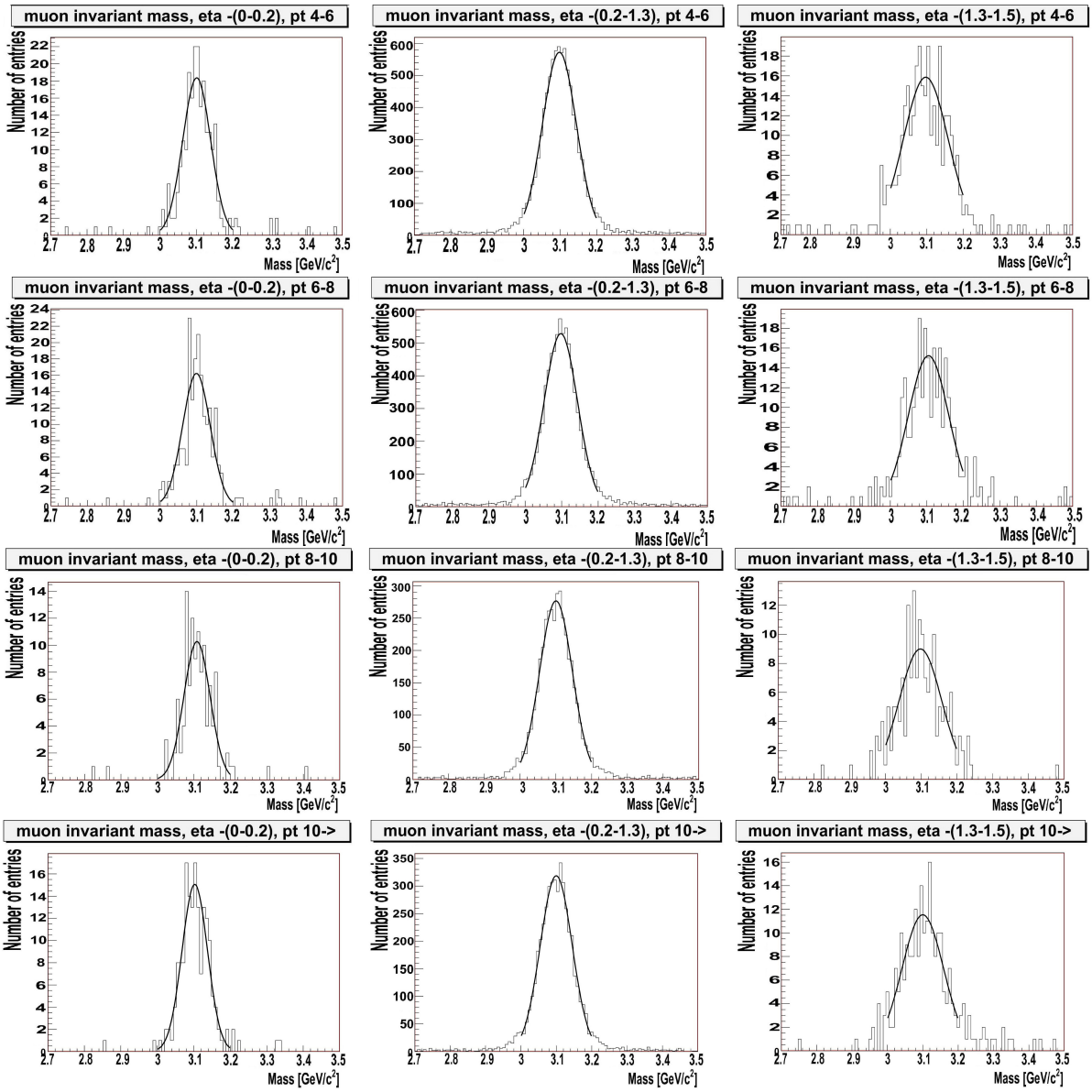
muon invariant mass, eta -(0-0.2), pt 4-6
muon invariant mass, eta -(0.2-1.3), pt 4-6
muon invariant mass, eta -(1.3-1.5), pt 4-6
muon invariant mass, eta -(0-0.2), pt 6-8
muon invariant mass, eta -(0.2-1.3), pt 6-8
muon invariant mass, eta -(1.3-1.5), pt 6-8
muon invariant mass, eta -(0-0.2), pt 8-10
muon invariant mass, eta -(0.2-1.3), pt 8-10
muon invariant mass, eta -(1.3-1.5), pt 8-10
muon invariant mass, eta -(0-0.2), pt 10->
muon invariant mass, eta -(0.2-1.3), pt 10->
muon invariant mass, eta -(1.3-1.5), pt 10->
Number of entries
Mass [GeV/c²]

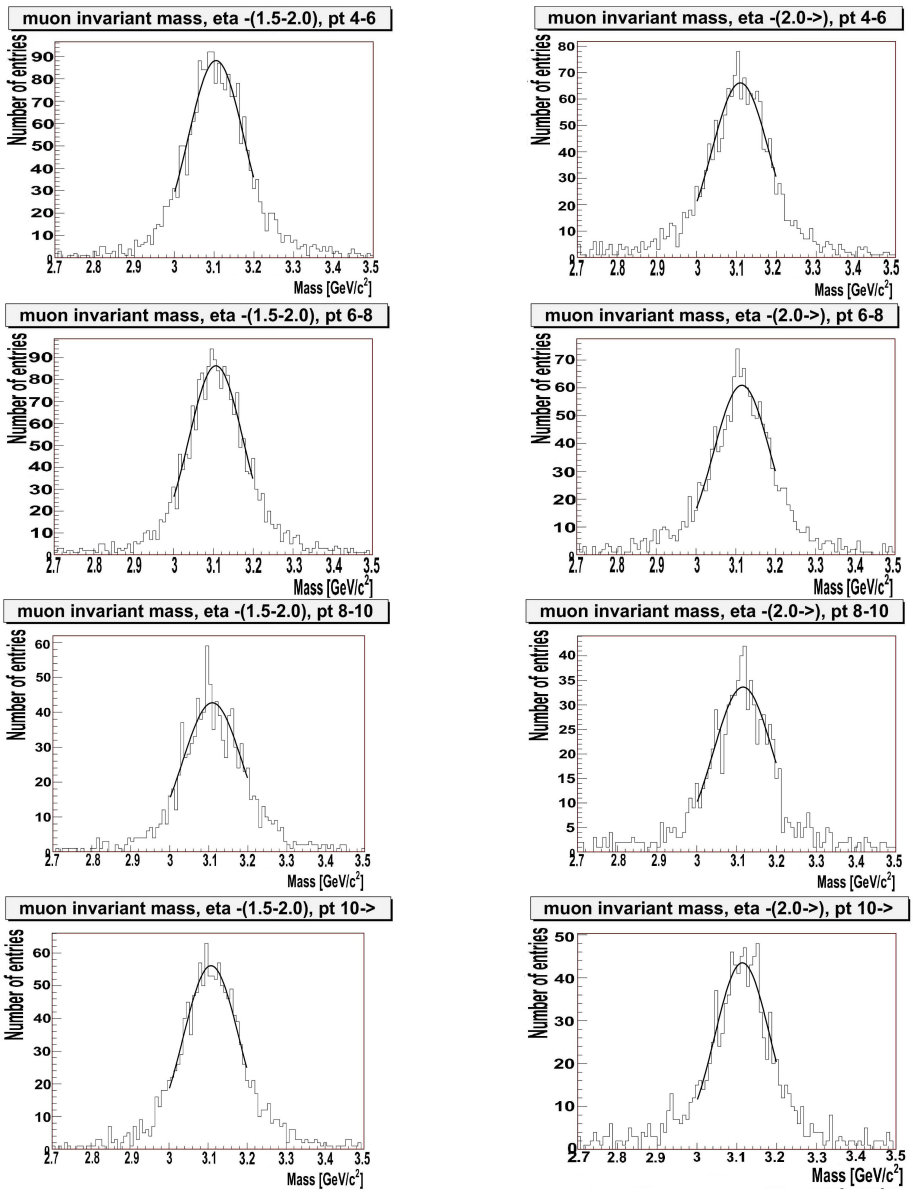

Figure 5.2: Reconstructed J/ψ mass obtained from muons in different regions of negative η (decreases from the left column of the previous page to the right column of this page) and with different p_T values (increases from the top row to the bottom row). The solid line shows the Gaussian fit.

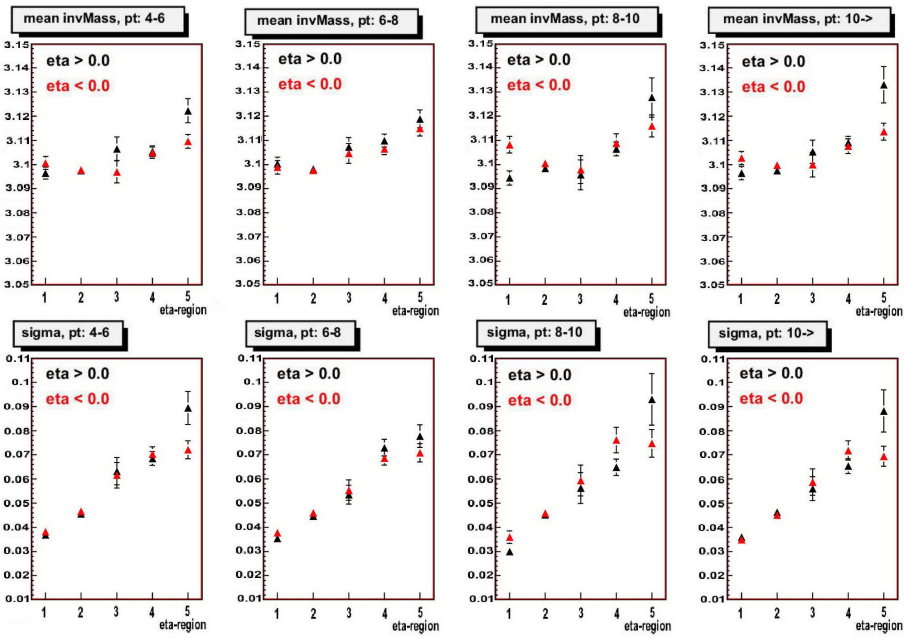

Figure 5.3: Summary of the fit results from Figure 5.2 and from a similar collection of plots for regions of positive η. The first (second) row depicts the mean value (standard deviation) for the four p_T-intervals. The fit values for the positive (negative) η-regions are shown as black (red) triangles, and the regions are defined by 5.2. The error bars (in most cases hidden by the marker) represent the errors from the fit.

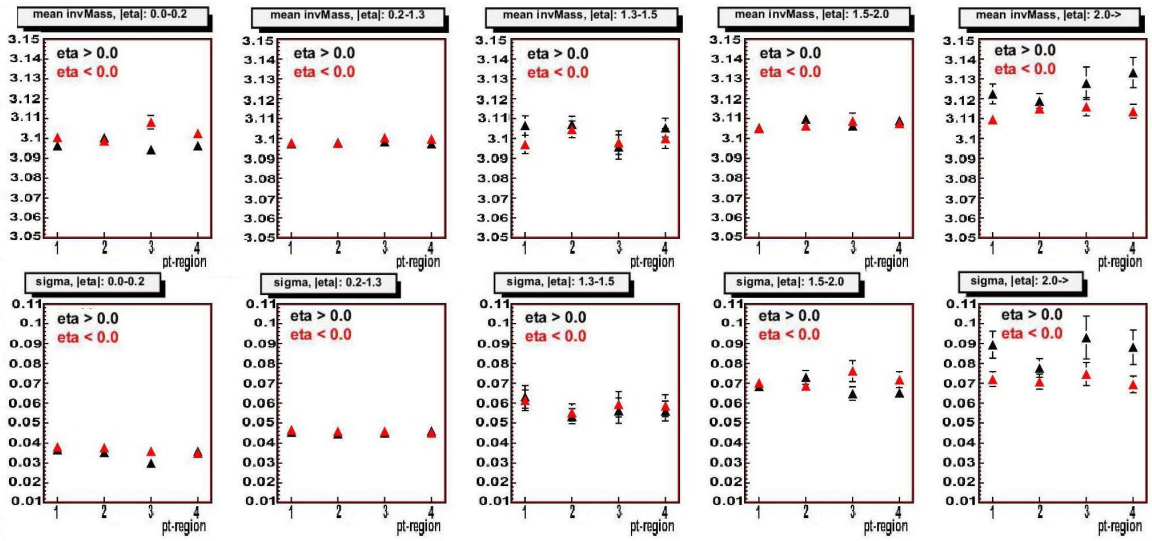

Figure 5.4: Summary of the fit results from Figure 5.2 and from a similar collection of plots for regions of positive η. The first (second) row depicts the mean value (standard deviation) for the five $|\eta|$-regions. The fit values for the positive (negative) η-regions are shown as black (red) triangles, and the p_T-regions on the x-axis are defined by 5.3. The error bars (in most cases hidden by the marker) represent the errors from the fit.

		Mean [GeV/c^2]		Sigma [GeV/c^2]	
p_T interval	**η interval**	**Pos. η**	**Neg. η**	**Pos. η**	**Neg. η**
[4,6)	[0,0.2)	3.096(2)	3.101(3)	0.03682(192)	0.03814(207)
	[0.2,1.3)	3.097(1)	3.098(1)	0.04555(047)	0.04666(050)
	[1.3,1.5)	3.107(5)	3.097(5)	0.06318(567)	0.06152(521)
	[1.5,2.0)	3.105(2)	3.105(2)	0.06850(281)	0.07032(302)
	[2.0,→)	3.122(5)	3.110(3)	0.08941(684)	0.07212(372)
[6,8)	[0,0.2)	3.100(3)	3.099(3)	0.03583(200)	0.03779(218)
	[0.2,1.3)	3.098(1)	3.098(1)	0.04466(047)	0.04598(051)
	[1.3,1.5)	3.107(4)	3.105(4)	0.05351(387)	0.05535(424)
	[1.5,2.0)	3.110(3)	3.106(2)	0.07298(345)	0.06868()289
	[2.0,→)	3.119(4)	3.115(3)	0.07772(470)	0.07086(374)
[8,10)	[0,0.2)	3.094(3)	3.108(3)	0.02997(214)	0.03590(261)
	[0.2,1.3)	3.098(1)	3.100(1)	0.04513(068)	0.04586(070)
	[1.3,1.5)	3.096(6)	3.098(6)	0.05623(639)	0.05941(641)
	[1.5,2.0)	3.106(3)	3.109(4)	0.06486(341)	0.07615(529)
	[2.0,→)	3.128(8)	3.116(5)	0.09301(1070)	0.07469(573)
[10,→)	[0,0.2)	3.096(3)	3.103(3)	0.03588(208)	0.03485(207)
	[0.2,1.3)	3.097(1)	3.100(1)	0.04618(065)	0.04505(063)
	[1.3,1.5)	3.105(5)	3.100(5)	0.05605(495)	0.05871(551)
	[1.5,2.0)	3.109(3)	3.108(3)	0.06533(308)	0.07179(399)
	[2.0,→)	3.133(8)	3.114(3)	0.08817(870)	0.06940(420)

Table 5.1: Fit-parameters extracted from the different J/ψ mass plots in Figure 5.2, plus the corresponding numbers for the positive regions of η. The numbers in parenthesis are the errors on the last digits. The values are displayed graphically in Figures 5.3 and 5.4.

5.3 Mass Variations with Changes in Azimuthal Angle

So far we have only investigated different pseudorapidity regions in the detector. To improve our understanding of the whole detector, we now include the azimuthal angle in our analysis. The reconstruction efficiency as a function of ϕ is shown in Figure 5.5. The Dips around $\phi = 0.8$ and 2.2 are most likely due to the extra material introduced by

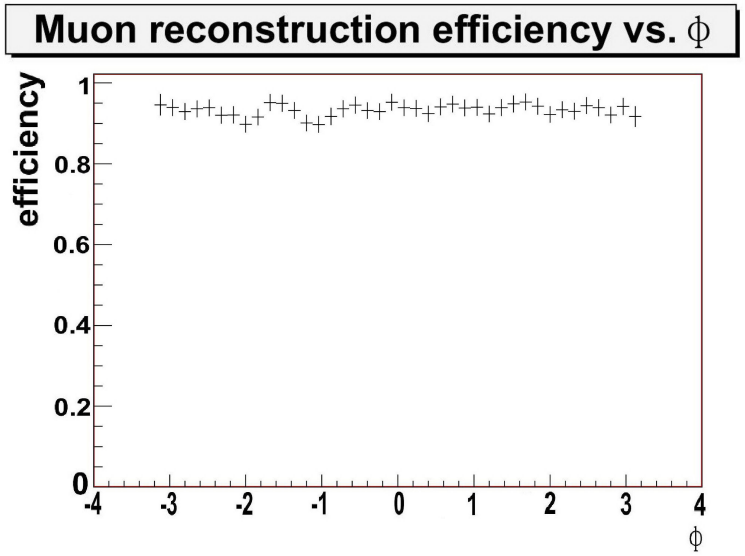

Figure 5.5: The muon reconstruction efficiency as a function of ϕ. The dips around ϕ = -1.0 and -2.0 are most likely due to the extra material introduced because of the detector's support structure.

the detector's support structure.

Since we already concluded that variations in the muon momenta did not have any perceivable effect on the reconstruction efficiency, we are free to reconstruct the J/ψ mass without any additional requirement than that the two muons are located in the same ϕ region. Combined with the fact that the muons are expected to be evenly distributed over the azimuthal angle space, this means that we can divide the detector into finer slices before the statistics become too limited. The regions are defined as

$$|\phi| \in [0, 0.2), [0.2, 0.4), [0.4, 0.6), \ldots, [2.8, 3.0), [3.0, \rightarrow) \,, \tag{5.4}$$

where we in addition distinguish between positive and negative values of ϕ. After reconstructing the invariant mass for the different regions (see Figure 5.6 for examples), we impose a Gaussian fit (Equation 4.3) over the interval [3.0 GeV,3.2 GeV] and extract the fit-parameters. Table 5.2 lists the obtained values, while Figure 5.7 provides a graphical representation.

Only small mass fluctuations are visible, which means that the asymmetry we observed in the efficiency plot seems to have no effect on the mass reconstruction. This

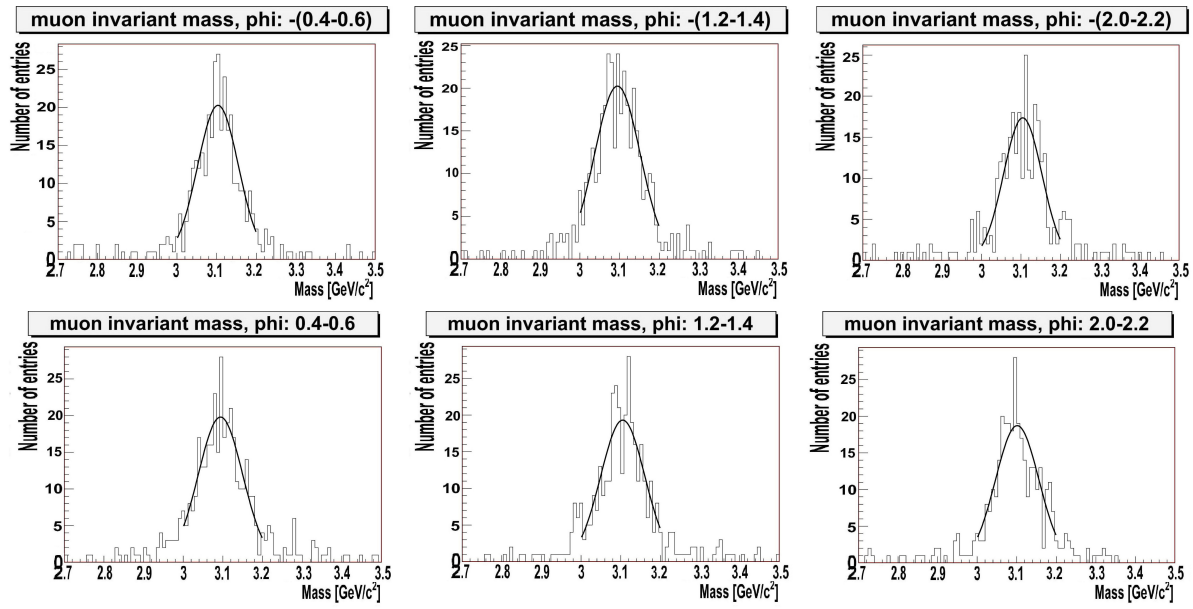

Figure 5.6: Examples of the reconstructed J/ψ mass for various regions of ϕ. The top row shows the fitted spectrum for regions 3, 7, and 11 of negative ϕ, while the bottom row shows the equivalent regions of positive ϕ.

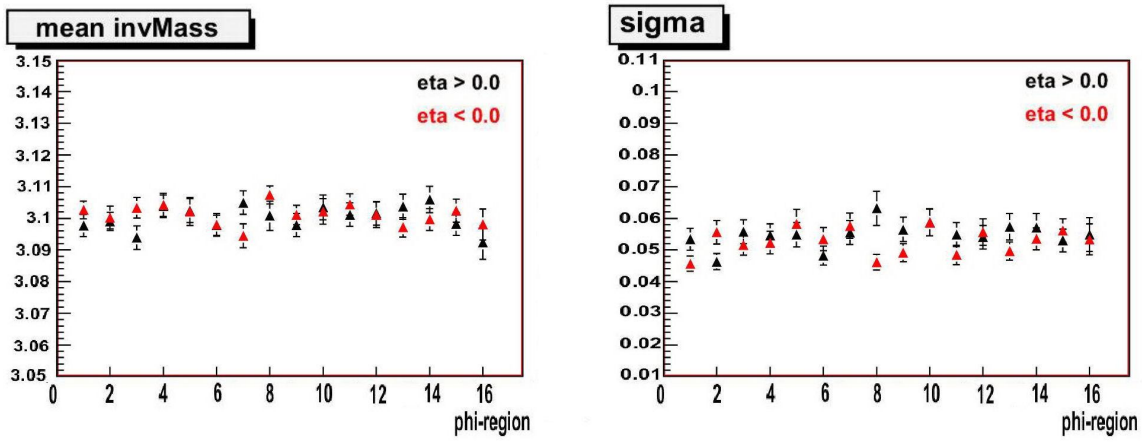

Figure 5.7: Summary of the mean (left) and the standard deviation (right) obtained for the various regions of ϕ. The fit values for the positive (negative) ϕ-regions are shown as black (red) triangles, and the ϕ-regions on the x-axis are defined by 5.4. The error bars represent the errors from the fit.

	Mean [GeV/c^2]		**Sigma [GeV/c^2]**	
ϕ interval	**Pos. ϕ**	**Neg. ϕ**	**Pos. ϕ**	**Neg. ϕ**
[0.0,0.2)	3.098(4)	3.103(3)	0.05337(350)	0.04564(243)
[0.2,0.4)	3.099(3)	3.100(4)	0.04633(255)	0.05559(372)
[0.4,0.6)	3.094(4)	3.103(3)	0.05574(378)	0.05159(319)
[0.6,0.8)	3.104(4)	3.104(4)	0.05464(365)	0.05229(359)
[0.8,1.0)	3.102(4)	3.102(4)	0.05481(386)	0.05822(464)
[1.0,1.2)	3.098(3)	3.098(4)	0.04823(294)	0.05344(359)
[1.2,1.4)	3.105(4)	3.094(4)	0.05549(379)	0.05764(401)
[1.4,1.6)	3.101(5)	3.107(3)	0.06316(537)	0.04614(252)
[1.6,1.8)	3.098(4)	3.101(3)	0.05647(381)	0.04916(285)
[1.8,2.0)	3.103(4)	3.102(4)	0.05877(429)	0.05866(424)
[2.0,2.2)	3.101(4)	3.104(3)	0.05484(375)	0.04846(307)
[2.2,2.4)	3.102(4)	3.101(4)	0.05405(375)	0.05565(421)
[2.4,2.6)	3.104(4)	3.097(3)	0.05736(417)	0.04965(287)
[2.6,2.8)	3.106(4)	3.100(3)	0.05709(438)	0.05350(342)
[2.8,3.0)	3.098(4)	3.102(4)	0.05301(361)	0.05612(376)
[3.0,→)	3.092(5)	3.098(5)	0.05487(539)	0.05333(487)

Table 5.2: Mean and sigma obtained from Gaussian fits of the J/ψ mass for different regions of ϕ. The numbers in parenthesis are the errors on the last digits. The values are displayed graphically in Figure 5.7.

means that we do not have to separate between positive and negative values of ϕ, and we can also make the regions bigger (and improve the statistics) without loosing information. From Figure 5.6 it is clear that this is necessary if we try to look at η and ϕ combined. The reason for wanting to do this is mainly to make the analysis more efficient. Unfortunately, the problem regions in η dictates that we still need more statistics before this can be done.

5.4 Possible extensions

The analysis performed here only investigates the possibility of material and structural effects on the mass reconstruction. A planned addition to the study is to investigate the effects of a varying magnetic field. A good description of the magnetic field, and how it varies throughout the detector volume, is in this case essential. When we start looking at collision data, the magnetic field will always be present, and a good understanding of its effect on the reconstruction will be necessary.

Chapter 6

Conclusion

In this thesis we have reconstructed the mass of the B_s meson using simulated $B_s \rightarrow J/\psi\phi \rightarrow \mu^+\mu^- K^+ K^-$ events from the official ATLAS production. Two separate types of backgrounds have been explored, and we have shown that by applying some simple selection criteria, we can separate these from the signal. The obtained mass after an optimized selection was (5376.2 $\pm$ 2.6) MeV with a (58.6 $\pm$ 2.4) Mev standard deviation. This is higher than the current PDG value of (5366.3 $\pm$ 0.6) MeV [17], but the discrepancy is caused by an over-correction in the muon reconstruction algorithms and is not an error of this analysis.

A separate validation study was also performed. Here we used simulated $J/\psi \rightarrow \mu^+\mu^-$ events and looked for variations in the invariant mass distribution for various regions of the detector. It was shown that the mass increases at larger values of $|\eta|$, while only minor fluctuation were seen as a function of $|\phi|$. Possible extensions to this analysis were also discussed.

Bibliography

[1] B.R.Martin and G.Shaw, *Particle Physics*. John Wiley & Sons, 1992.

[2] W. M. Yao et al., "The review of particle physics", *Journal of Physics G: Nuclear and Particle Physics* **33** (2006), no. 1,.

[3] F. Mandl and G. Shaw, *Quantum Field Theory*. John Wiley & Sons, 1993.

[4] http://en.wikipedia.org/wiki/Quantum_field_theory.

[5] A. Raklev, "Groups, algebras and susy - an algebraic introduction to supersymmetry." notes from seminar held in Bergen, 2007.

[6] S. L. Glashow, "Partial symmetries of weak interactions", *Nuclear Physics* **22** (1961) 579.

[7] S. Weinberg, "A model of leptons", *Phys. Rev. Lett.* **19** (1967) 1264.

[8] A. Salam and J. C. Ward, "Electromagnetic and weak interactions", *Phys. Lett.* **13** (1964) 168.

[9] A. Salam, "Weak and electromagnetic interactions", in *Elementary Particle Theory*, N. Svartholm, ed., p. 367. Almquist and Wiksell, 1968.

[10] P. W. Higgs, "Broken symmetries, massless particles and gauge fields", *Phys. Lett.* **12** (1964) 132.

[11] P. W. Higgs, "Broken symmetries and the masses of gauge bosons", *Phys. Rev. Lett.* **13** (1964) 508.

[12] P. W. Higgs, "Spontaneous symmetry breakdown without massless bosons", *Phys. Rev.* **145** (1966) 1156.

[13] N. Cabibbo, "Unitary symmetry and leptonic decays", *Phys. Rev. Lett.* **10** (1963) 531.

[14] M. Kobayashi and T. Maskawa, "CP-violation in the renormalizable theory of weak interaction", *Progress of Theoretical Physics* **49** (1973).

[15] L. Maiani, "CP violation in purely lefthanded weak interactions", *Phys. Lett.* **B62** (1976) 183.

[16] L. Wolfenstein, "Parametrization of the Kobayashi-Maskawa matrix", *Phys. Rev. Lett.* **51** (1983) 1945.

[17] C. Amsler et al., "The review of particle physics", *Phys. Lett.* **B667** (2008), no. 1,.

[18] J. H. Christenson, J. W. Cronin, V. L. Fitch, and R. Turlay, "Evidence for the 2π decay of the K_2^0 meson", *Phys. Rev. Lett.* **13** (1964) 138.

[19] A. Abashian, R. J. Abrams, D. W. Carpenter, G. P. Fisher, B. M. K. Nefkens, and J. H. Smith, "Search for CP nonconservation in K_2^0 decays", *Phys. Rev. Lett.* **13** (1964) 243.

[20] B. Aubert et al., [BABAR Collaboration], "Observation of CP violation in the B^0 meson system", *Phys. Rev. Lett.* **87** (2001). 091801.

[21] K. Abe et al., [BELLE Collaboration], "Observation of large CP violation in the neutral B meson system", *Phys. Rev. Lett.* **87** (2001). 091802.

[22] I. I. Bigi and A. I. Sanda, "Notes on the observability of CP violations in B decays", *Nuclear Physics* **B193** (1981) 85–108.

[23] A. J. Buras and R. Fleischer, "Quark mixing, CP violation and rare decays after the top quark discovery", 1997. hep-ph/9704376.

[24] A. F. Falk, "Introduction to hadronic B physics", 1998. hep:ph/9812217.

[25] Lecture notes on angular distributions in V-V decays, from course by Gerald Eigen.

[26] A. S. Dighe, I. Dunietz, H. J. Lipkin, and J. L. Rosner, "Angular distributions and lifetime differences in $B_s \to J/\psi\phi$ decays", *Phys. Lett.* **B369** (1996) 144–150. hep-ph/9511363.

[27] A. S. Dighe, I. Dunietz, and R. Fleischer, "Extracting CKM phases and $B_s - \bar{B}_s$ mixing parameters from angular distributions of non-leptonic B decays", *Eur. Phys. J. C* **6** (1999) 647–662. DOI 10.1007/s100529800954.

[28] http://public.web.cern.ch/public/en/About/History-en.html.

[29] ATLAS Collaboration, "The ATLAS Experiment at the CERN Large Hadron Collider", tech. rep., CERN, 2007.

[30] M. Benedikt et al., "LHC Design Report, Vol. 1-3", tech. rep., CERN, 2004. http://ab-div.web.cern.ch/ab-div/Publications/LHC-DesignReport.html.

[31] K. Hübner, "The accelarators", in *50 Years of Research at CERN: From Past to Future*, G. Giudice, ed., pp. 1–27. May, 2005.

[32] B. Povh, K. Rith, C. Scholtz, and F. Zetsche, *Particles and Nuclei: An Introduction to the Physical Concepts*. Springer, 4 ed., 2004.

[33] ATLAS Collaboration. http://cdsweb.cern.ch/record/39038.

[34] ATLAS Collaboration, "ATLAS Detector and Physics Performance, Technical Design Report, Vol. 1", tech. rep., CERN, 1999.

[35] http://en.wikipedia.org/wiki/Pseudorapidity.

[36] ATLAS Collaboration. http://atlas.ch/inner_detector.html.

[37] J. Colas et al., "Position resolution and particle identification with the ATLAS EM calorimeter", *Nucl. Instrum. Methods Phys. Res.* (May, 2005) 96–115. physics/0505127.

[38] ATLAS Collaboration. http://atlas.ch/muon.html.

[39] G. Duckeck et al., "ATLAS Computing Technical Design Report", tech. rep., CERN, 2005. http://doc.cern.ch//archive/electronic/cern/preprints/lhcc/public/lhcc-2005-022.pdf.

[40] M. Dobbs, S. Frixione, E. Laenen, and K. Tollefson, eds., *Les Houches Guidebook to Monte Carlo Generators for Hadron Collider Physics*. 2004. hep-ph/0403045.

[41] T. S. strand, L. Lönnblad, S. Mrenna, and P. Skands, *PYTHIA 6.3 Physics and Manual*. 2003. hep-ph/0308153.

[42] G. C. et al., ed., *HERWIG 6.5: an event generator for Hadron Emission Reactions With Interfering Gluons (including supersymmetric processes)*. 2002. hep-ph/0011363.

[43] http://www.hep.ucl.ac.uk/atlas/atlfast.

[44] Geant4 Web page: http://cerrn.ch/geant4.

[45] Geant4 Collaboration (S. Agostinelli et al.), "Geant4 - A Simulation Toolkit", *Nuclear Instruments and Methods in Physics Research* **A 506** (2003) 250–303.

[46] https://twiki.cern.ch/twiki/bin/view/Atlas/WorkBookFullChain.

[47] "Analyses model report", tech. rep., ATLAS, CERN, Jan., 2008.

[48] P. Mato, "Gaudi-architecture design document", Tech. Rep. LHCb-98-064, CERN, Geneva, Nov., 1998.

[49] https://twiki.cern.ch/twiki/bin/view/Atlas/WorkBookAthenaFramework.

[50] https://twiki.cern.ch/twiki/bin/view/Atlas/WorkBook.

[51] R. Brun, F. Rademakers, P.Canal, I. Antcheva, and D. Buskulic, *ROOT User's Guide 5.16*, 2007. http://root.cern.ch/root/doc/Users_Guide_5_16_TwoInOne.pdf.